A discrete representation of material heterogeneity for the finite-difference modelling of seismic wave propagation in a poroelastic medium

Peter Moczo [1,2] , David Gregor [1] , Jozef Kristek [1,2] , Josep de la Puente [3]

[1] *Faculty of Mathematics, Physics and Informatics, Comenius University Bratislava, Mlynska dolina F1, 842 48 Bratislava, Slovak Republic. E-mail: moczo@fmph.uniba.sk*

[2] *Earth Science Institute, Slovak Academy of Sciences, Dubravska cesta 9, 845 28 Bratislava, Slovak Republic*

[3] *Barcelona Supercomputing Center, Nexus II – Planta 3C, Jordi Girona 29, 08034 Barcelona, Spain*

SUMMARY

As recently demonstrated the most advanced finite-difference schemes are sufficiently efficient and accurate numerical-modelling tools for seismic wave propagation and earthquake ground motion especially in local surface sedimentary structures. The key advantages of the explicit finite-difference schemes are a uniform grid, no matter what positions of material interfaces are in the grid, and one scheme for all interior points, no matter what their positions are with respect to the material interfaces. Efficiency and accuracy is determined by the grid dispersion and discrete representation of a material heterogeneity. After having developed discrete representations for the elastic and viscoelastic media, we present here a new discrete representation of material heterogeneity in the poroelastic medium. The representation is capable of sub-cell resolution and makes it possible to model an arbitrary shape and position of an interface in the grid. At the same time, the structure and thus the number of operations in the finite-difference scheme is unchanged compared to the homogeneous or smoothly heterogeneous medium.

Key words
Computational seismology; Theoretical seismology; Wave propagation; Numerical approximations and analysis; Poroelastic medium

1 INTRODUCTION

Motivation

There are two key advantages of the explicit finite-difference (FD) schemes: 1. the possibility to cover a computational domain with a uniform spatial grid no matter what positions of material interfaces are in the grid, 2. the possibility to apply one scheme to all interior grid points (points not lying on a grid border) no matter what their positions are with respect to the material interface. Computational efficiency_and_accuracy are determined by the grid dispersion and the way how continuous and mainly discontinuous material heterogeneity (material interface) is

represented by values of material parameters assigned to grid points, that is, how the true continuum is represented in the discrete grid. Moczo et al. (2002, 2014), Kristek & Moczo (2003) and Kristek et al. (2017) developed the discrete representation of the material interface between two elastic and viscoelastic materials that is capable of subcell resolution and "sensing" an arbitrary shape and position of the interface in the grid. Extensive numerical modelling of seismic wave propagation and earthquake ground motion in canonical and complex realistic models confirmed that with the proper discrete representation of material heterogeneity the most advanced FD schemes can be more efficient in case of local surface sedimentary structures than the spectral-element and discontinuous-Galerkin methods (e.g., Chaljub et al. 2010, 2015; Maufroy et al. 2015).

A natural question is then whether a similarly accurate discrete representation of the material heterogeneity can be obtained also for the poroelastic medium.

As in the case of the elastic and viscoelastic media it is crucial to find a representation that is both sufficiently accurately (though approximately) consistent with boundary conditions at the interface as well as computationally efficient. In the case of the elastic and viscoelastic media the orthorhombic representation is such a sufficiently accurate approximation that does not increase the number of non-zero elements of the stiffness matrix (and thus neither the number of algebraic operations in calculation of stress) compared to the smoothly heterogeneous medium.

In this article we explore a similar approach in the case of poroelastic media. Both the equations of motion and constitutive equations of the poroelastic media are considerably more complex than those for the elastic medium. Consequently, the problem is not trivial and it is hard to intuitively guess what we can expect.

Previous studies on FD modelling in the porous medium

The FD method has been used for modelling wave propagation in the elastic medium since late 60s – probably the best known example being the article by Alterman & Karal (1968). The method was applied for simulating wave propagation in the porous medium later. One of the first studies was the article by Garg et al. (1974) who investigated propagation of compressional waves in fluid-saturated elastic porous media using the computer code POROUS (Riney et al. 1972, 1973).

More studies applying the FD method appeared in the 90s. Hassanzadeh (1991) used it to solve the Biot's poroacoustic equations in a homogeneous fluid-saturated porous medium. Zhu & McMechan (1991) developed a 2nd-order explicit conventional FD scheme, following Kelly et al. (1976), for solving the Biot's poroelastic equations in a homogeneous porous medium. Dai et al.

(1995) extended the FD method to Biot's poroelastic wave equations in 2D heterogeneous porous media. Considering a 1st-order hyperbolic system equivalent to Biot's equations, they developed a MacCormack predictor-corrector (4, 2) scheme (4th-order accurate in space and 2nd-order accurate in time), based on a spatial splitting technique. The scheme on the collocated grid updates the vector consisting of the solid and fluid particle-velocity components, the solid stress-tensor components, and the fluid pressure.

Schemes used by Hassanzadeh (1991) and Zhu and McMechan (1991) are based on the homogeneous approach - wave equations for each homogeneous layer are solved separately and the boundary conditions must be satisfied explicitly on the interfaces between different layers. Dai et al. (1995) applied the heterogeneous approach – one scheme is used for all interior grid points and the heterogeneity of medium is accounted for by values of material parameters assigned to the grid positions. Dai et al. explicitly said about the heterogeneous approach what was then considered correct: the boundary conditions are satisfied implicitly and more complicated geometries can be accommodated with no extra effort. It has been later recognized that this is not so (Moczo et al. 2002, 2014; Kristek et al. 2017).

Zhang (1999) developed a quadrangle-grid velocity-stress FD scheme for simulating wave propagation in 2D heterogeneous porous media. In his non-orthogonal spatial grid, two solid particle-velocity components and two components of velocity of the pore fluid relative to that of the solid share one grid position whereas the three solid stress-tensor components and the fluid pressure share another grid position. Apart from the non-orthogonal geometry and fluid-related field quantities, the grid is the partly-staggered grid (first used by Andrews in 1973 and later called by Saenger and his collaborators rotated staggered grid).

Zeng et al. (2001) applied the perfectly matched layer in their FD numerical modelling of wave propagation in poroelastic media. Wang et al. (2003) improved efficiency of the FD modelling of wave propagation in poroelastic media by developing an (8, 2) explicit velocity-stress staggered-grid (SG) scheme. Wang et al. (2003) pointed out, referring to Levander (1988), that with the SG schemes strong velocity-contrast interfaces can be handled with high accuracy because derivatives of material parameters are not required. As already mentioned, the representation of interfaces seems easy and implicit with the heterogeneous schemes solving the first-order equations of motion but, in fact, it is not the case – again we refer to Moczo et al. (2002, 2014) and Kristek et al. (2017).

Saenger et al. (2004) applied the rotated staggered FD grid (the basic variant of the partly-staggered grid) technique to calculate elastic wave propagation in 3D porous media. Saenger et

al. (2005) extended the approach to porous media saturated with a Newtonian (viscous) fluid using a generalized Maxwell body.

Sheen et al. (2006) presented a parallel implementation of the 2D P-SV velocity-stress SG FD scheme, 4th-order in space and 2nd-order in time, for fluid-saturated poroelastic media. They also addressed the aspect of the effective media parameters. They averaged shear modulus according to Graves (1996). They applied harmonic averaging to density, effective fluid density, fluid density and mobility of the fluid. Harmonic averaging of density, however, violates the boundary conditions at an interface (Moczo et al. 2002). The authors correctly suggest the need to properly address the problem of the effective grid material parameters in the subsequent research.

Masson et al. (2006) applied a 2D (4, 2) velocity-stress SG FD scheme. They analysed stability conditions and demonstrated that over a wide range of porous material properties typical of sedimentary rock and despite the presence of fluid pressure diffusion (Biot slow waves), the usual Courant condition governs the stability as if the problem involved purely elastic waves. In relation to our study we may note that they averaged shear modulus according to Graves (2006). Masson & Pride (2007) applied FD modelling to investigate seismic attenuation and dispersion due to mesoscopic-scale heterogeneity. Specifically, they simulated one loss mechanism that can be important across the seismic band of frequencies when heterogeneity is present within fluid-saturated porous samples.

Krzikalla & Müller (2007a, b) applied the rotated spatial FD operators (Saenger et al. 2000) to improve stability in modelling high-contrast materials compared to standard SG scheme. Wenzlau & Müller (2009) implemented a velocity-stress FD scheme for modelling wave propagation and diffusion in porous media. The scheme is 2nd-order accurate in time and includes high-order spatial differentiation operators, and is parallelized using the domain-decomposition technique. The spatial discretization combines the standard and rotated SG operators. Wenzlau & Müller presented several tests to estimate the accuracy of poroelastic wave-propagation schemes for the high-frequency case where the Biot slow wave is a propagating wave mode and for the low-frequency case when this wave mode becomes diffusive. They introduced a diffusion wavelength in relation to the numerical dispersion. They also addressed the stability for strongly heterogeneous medium and compared the standard and rotated staggered-grid schemes. Masson & Pride (2010) expanded their scheme to Biot's equations across all frequencies. O'Brien (2010) presented 3D (4, 2) standard and rotated SG schemes. They analysed stability and numerical dispersion.

Chiavassa & Lombard (2011, 2013) made an important contribution to numerical modelling of wave propagation in heterogeneous 2D fluid/poroelastic media mainly by applying an immersed interface method to discretize the interface conditions and to introduce a subcell resolution. They also implemented a 4th-order ADER scheme with Strang splitting for time-marching, and a space-time mesh-refinement to capture the slow compressional wave. With respect to the discontinuous material heterogeneity the immersed-interface method is the most sophisticated approach applied so far. Arbitrary-shaped interfaces can be handled and accuracy is ensured by a subcell resolution on a Cartesian grid. Its only disadvantage is the relatively high computational cost.

Chiavassa & Lombard (2013) made this explicit statement: "… arbitrary-shaped geometries with various interface conditions … are badly discretized by FD methods on Cartesian grids". Well, the "FD methods" is in fact a large family of FD schemes differing strongly in their accuracy and efficiency. The statement by Chiavasa & Lombard is relevant mainly for those FD modellers who were misled by the absence of derivatives of material parameters in the velocity-stress or displacement-stress formulation of the equation of motion and constitutive relation. Those modellers assumed that boundary conditions are implicitly satisfied at boundaries. Consequently, majority of the FD schemes for seismic wave propagation had been using for years grid material parameters inconsistent with the boundary conditions at the interface; see Moczo et al. (2014).

Blanc (2013) presented a numerical approach to the complete Biot-DA (diffusive approximation) system in which the equations of evolution are split into two parts: a propagative part is discretized using a 4th-order FD scheme, and a diffusive part is solved exactly. She also implemented the immersed-interface method to account for the jump conditions and for the geometry of the interfaces on a Cartesian grid.

Yang & Mao (2017) presented simulation of seismic wave propagation in 2D poroelastic media using weighted-averaging FD stencils in the frequency–space domain. Their scheme is an extension of the 25-point weighted-averaging FD scheme proposed by Min et al. (2000). They used the optimal weighting coefficients in order to account for medium heterogeneity without rotating the coordinate system and the grid points.

For further reading on computational poroelasticity and numerical modelling we refer to review by Carcione et al. (2010) and Yang & Mao (2017).

Structure of this article

We first recall the constitutive relations for the poroelastic medium and boundary conditions at a material interface between poroelastic media. Then we analyse the constitutive relation at a planar material interface parallel with a grid plane. Based on the analysis, we eventually present approximate grid-cell averaging of material parameters appearing in the constitutive relations. We continue with the equations of motion. After addressing the planar interface parallel with a grid plane we present grid-cell averaging of material parameters appearing in the equations of motion. We then test the developed discrete representation numerically by comparing our seismograms with seismograms calculated by the exact method developed by Diaz & Ezziani (2008). Eventually we present comparison of our seismograms with the discontinuous Galerkin method for a complex model.

In this article we address the 2D problem. It is, however, straightforward to extend the approach and, in fact, directly the resulting discrete representation, to the 3D problem.

2 CONSTITUTIVE LAW AND EQUATIONS OF MOTION FOR A 2D POROELASTIC MEDIUM

A comprehensive introduction and theory of wave propagation in the porous media is given, e.g., in the book by Carcione (2015), review article by Carcione et al. (2010) and comprehensive article by Morency and Tromp (2008). Formulation of equations for the 2D P-SV problem may be found in, e.g., articles by Carcione (1998) and Carcione & Helle (1999).

The constitutive equations for 2D P-SV problem in a smoothly heterogeneous isotropic poroelastic medium may be written as

$$
\begin{bmatrix} \sigma_{xx} \\ \sigma_{zz} \\ \sigma_{xz} \\ -p \end{bmatrix} = \begin{bmatrix} \Lambda + \alpha^2 M & \lambda + \alpha^2 M & 0 & \alpha M \\ \lambda + \alpha^2 M & \Lambda + \alpha^2 M & 0 & \alpha M \\ 0 & 0 & 2\mu & 0 \\ \alpha M & \alpha M & 0 & M \end{bmatrix} \begin{bmatrix} \varepsilon_{xx} \\ \varepsilon_{zz} \\ \varepsilon_{xz} \\ \varepsilon_w \end{bmatrix} \tag{2.1}
$$

where σ_{xx}, σ_{zz} and σ_{xz} are the total stress-tensor components, p is the fluid pressure, ε_{xx}, ε_{zz} and ε_{xz} are the solid matrix strain-tensor components, $\varepsilon_w \equiv w_{k,k} = w_{x,x} + w_{z,z}$, w_x and w_z are components of the displacement of the fluid relative to the solid frame, $\Lambda \equiv \lambda + 2\mu$, λ and μ are Lamé elastic coefficients of the solid matrix, α is the poroelastic coefficient of effective stress and M is the coupling modulus between the solid and fluid.

It may be convenient to rewrite the constitutive equations in the following form:

$$\sigma_{xx} = \Lambda\,\varepsilon_{xx} + \lambda\varepsilon_{zz} - \alpha p$$
$$\sigma_{zz} = \lambda\,\varepsilon_{xx} + \Lambda\varepsilon_{zz} - \alpha p$$
$$p = -\alpha M\,\varepsilon_{xx} - \alpha M\,\varepsilon_{zz} - M\,\varepsilon_w$$
$$\sigma_{xz} = 2\mu\varepsilon_{xz}$$

(2.2)

3 BOUNDARY CONDITIONS AT A MATERIAL INTERFACE

Consider an interface between two materials indicated by the $^{+}$ and $^{-}$ superscripts. The boundary conditions at an interface between two poroelastic media (Deresiewicz & Skalak 1963, Lovera 1987, Gurevich & Schoenberg 1999; for the overview see Carcione 2015) require continuity of the (a) traction vector, (b) fluid pressure, (c) solid displacement vector and (d) normal component of the relative fluid displacement vector. These conditions may be written as

$$\sigma_{ij}^{+} n_j = \sigma_{ij}^{-} n_j$$
$$p^{+} = p^{-}$$
$$u_i^{+} = u_i^{-}$$
$$w_i^{+} n_i = w_i^{-} n_i$$

(3.1)

where n_i is the unit normal to the interface and u_i solid displacement vector. Einstein's summation convention for repeating indices is assumed.

Consider a planar interface. The boundary conditions imply for the interface perpendicular to the x axis

$$\sigma_{xx} = \sigma_{xx}^{+} = \sigma_{xx}^{-}$$
$$\sigma_{xz} = \sigma_{xz}^{+} = \sigma_{xz}^{-}$$
$$\varepsilon_{zz} = \varepsilon_{zz}^{+} = \varepsilon_{zz}^{-}$$
$$p = p^{+} = p^{-}$$

(3.2)

and for the interface perpendicular to the z axis

$$\sigma_{zz} = \sigma_{zz}^{+} = \sigma_{zz}^{-}$$
$$\sigma_{xz} = \sigma_{xz}^{+} = \sigma_{xz}^{-}$$
$$\varepsilon_{xx} = \varepsilon_{xx}^{+} = \varepsilon_{xx}^{-}$$
$$p = p^{+} = p^{-}$$

(3.3)

The other quantities are discontinuous.

Let us note that this article does not address the problem of the traction-free surface.

4 STRESS-STRAIN RELATION FOR A PLANAR MATERIAL INTERFACE

We will derive stress-strain relations for a planar material interface parallel with a Cartesian coordinate plane. We will assume that the planar interface separates two homogeneous poroelastic halfspaces in contact.

4.1. Shear stress-tensor component at a planar interface perpendicular to the x axis

For the two halfspaces (indicated by the $^+$ and $^-$ superscripts) in a contact we may write in general

$$\sigma_{xz} = 2\mu^- \, \varepsilon_{xz}^- \quad , \quad \sigma_{xz} = 2\mu^+ \, \varepsilon_{xz}^+ \qquad (4.1)$$

or

$$\frac{1}{\mu^-} \, \sigma_{xz} \; = \; 2\,\varepsilon_{xz}^- \quad , \quad \frac{1}{\mu^+} \, \sigma_{xz} \; = \; 2\,\varepsilon_{xz}^+ \qquad (4.2)$$

Considering continuity of σ_{xz} and an arithmetic average $\left\langle \varepsilon_{xz} \right\rangle^x$ at the interface,

$$\left\langle \varepsilon_{xz} \right\rangle^x \; \equiv \; \tfrac{1}{2}\left(\varepsilon_{xz}^- + \varepsilon_{xz}^+ \right) \qquad (4.3)$$

the summation of Eqs. (4.2) leads to relation

$$\sigma_{xz} \; = \; 2\left\langle \mu \right\rangle^{Hx} \left\langle \varepsilon_{xz} \right\rangle^x \qquad (4.4)$$

with the harmonic average of the shear moduli

$$\left\langle \mu \right\rangle^{Hx} \equiv \frac{2}{\dfrac{1}{\mu^-} + \dfrac{1}{\mu^+}} \qquad (4.5)$$

Thus, continuity of σ_{zx} and the arithmetic averaging of the discontinuous ε_{zx} imply the harmonic averaging of the shear moduli, $\left\langle \mu \right\rangle^{Hx}$, in the stress-strain relation at the interface. Relation (4.4) has the same form as the fourth relation in (2.2), respectively, for a point in a smooth medium and is consistent with the interface boundary conditions. Relation (4.4) is the same as in the case of the interface between two elastic media.

4.2. Normal stress-tensor components at a planar interface perpendicular to the x axis

It follows from (2.2) that for two halfspaces in contact we may write

$$\sigma_{xx} = \Lambda^- \varepsilon_{xx}^- + \lambda^- \varepsilon_{zz} - \alpha^- p$$
$$\sigma_{xx} = \Lambda^+ \varepsilon_{xx}^+ + \lambda^+ \varepsilon_{zz} - \alpha^+ p \tag{4.6}$$

Relations (4.6) may be written as

$$\varepsilon_{xx}^- = \frac{1}{\Lambda^-} \sigma_{xx} - \frac{\lambda^-}{\Lambda^-} \varepsilon_{zz} + \frac{\alpha^-}{\Lambda^-} p$$
$$\varepsilon_{xx}^+ = \frac{1}{\Lambda^+} \sigma_{xx} - \frac{\lambda^+}{\Lambda^+} \varepsilon_{zz} + \frac{\alpha^+}{\Lambda^+} p \tag{4.7}$$

Continuity of σ_{xx}, ε_{zz} and p, and the arithmetic averaging of ε_{xx}^- and ε_{xx}^+ lead to

$$\langle \varepsilon_{xx} \rangle^x = \left(\langle \Lambda \rangle^{Hx} \right)^{-1} \sigma_{xx} - \left\langle \frac{\lambda}{\Lambda} \right\rangle^x \varepsilon_{zz} + \left\langle \frac{\alpha}{\Lambda} \right\rangle^x p \tag{4.8}$$

and

$$\sigma_{xx} = \langle \Lambda \rangle^{Hx} \langle \varepsilon_{xx} \rangle^x + \left\langle \frac{\lambda}{\Lambda} \right\rangle^x \langle \Lambda \rangle^{Hx} \varepsilon_{zz} - \left\langle \frac{\alpha}{\Lambda} \right\rangle^x \langle \Lambda \rangle^{Hx} p \tag{4.9}$$

For σ_{zz} we may write

$$\sigma_{zz}^- = \lambda^- \varepsilon_{xx}^- + \Lambda^- \varepsilon_{zz} - \alpha^- p$$
$$\sigma_{zz}^+ = \lambda^+ \varepsilon_{xx}^+ + \Lambda^+ \varepsilon_{zz} - \alpha^+ p \tag{4.10}$$

Before averaging σ_{zz}^- and σ_{zz}^+ we have to express ε_{xx}^- and ε_{xx}^+ using continuous field quantities. Using (4.7) in (4.10) we obtain

$$\sigma_{zz}^- = \frac{\lambda^-}{\Lambda^-} \sigma_{xx} + \left(\Lambda^- - \frac{\left(\lambda^-\right)^2}{\Lambda^-} \right) \varepsilon_{zz} - \left(\alpha^- - \frac{\alpha^- \lambda^-}{\Lambda^-} \right) p$$

$$\sigma_{zz}^+ = \frac{\lambda^+}{\Lambda^+} \sigma_{xx} + \left(\Lambda^+ - \frac{\left(\lambda^+\right)^2}{\Lambda^+} \right) \varepsilon_{zz} - \left(\alpha^+ - \frac{\alpha^+ \lambda^+}{\Lambda^+} \right) p \tag{4.11}$$

Continuity of σ_{xx}, ε_{zz} and p, and the arithmetic averaging of σ_{zz}^- and σ_{zz}^+ lead to

$$\langle \sigma_{zz} \rangle^x = \left\langle \frac{\lambda}{\Lambda} \right\rangle^x \sigma_{xx} + \left(\langle \Lambda \rangle^x - \left\langle \frac{\lambda^2}{\Lambda} \right\rangle^x \right) \varepsilon_{zz} - \left(\langle \alpha \rangle^x - \left\langle \frac{\lambda \alpha}{\Lambda} \right\rangle^x \right) p \tag{4.12}$$

Substituting the r.h.s. of Eq. (4.9) for σ_{xx} gives the final relation for σ_{zz}:

$$\langle\sigma_{zz}\rangle^x = \left\langle\frac{\lambda}{\Lambda}\right\rangle^x \langle\Lambda\rangle^{Hx} \langle\varepsilon_{xx}\rangle^x$$

$$+ \left[\langle\Lambda\rangle^x - \left\langle\frac{\lambda^2}{\Lambda}\right\rangle^x + \left(\left\langle\frac{\lambda}{\Lambda}\right\rangle^x\right)^2 \langle\Lambda\rangle^{Hx}\right]\varepsilon_{zz} \qquad (4.13)$$

$$- \left(\langle\alpha\rangle^x - \left\langle\frac{\alpha\lambda}{\Lambda}\right\rangle^x + \left\langle\frac{\alpha}{\Lambda}\right\rangle^x\left\langle\frac{\lambda}{\Lambda}\right\rangle^x\langle\Lambda\rangle^{Hx}\right)p$$

Thus, continuity of σ_{xx}, ε_{zz} and p, and the arithmetic averaging of the discontinuous ε_{xx} imply three averaged material coefficients: $\langle\Lambda\rangle^{Hx}$, $\left\langle\frac{\lambda}{\Lambda}\right\rangle^x\langle\Lambda\rangle^{Hx}$ and $\left\langle\frac{\alpha}{\Lambda}\right\rangle^x\langle\Lambda\rangle^{Hx}$. Continuity of

ε_{zz} and p, and the averaging of discontinuous σ_{zz} and ε_{xx} imply $\left\langle\frac{\lambda}{\Lambda}\right\rangle^x\langle\Lambda\rangle^{Hx}$ and two more

averaged coefficients:

$$\langle\Lambda\rangle^x - \left\langle\frac{\lambda^2}{\Lambda}\right\rangle^x + \left(\left\langle\frac{\lambda}{\Lambda}\right\rangle^x\right)^2\langle\Lambda\rangle^{Hx} \quad \text{and} \quad \langle\alpha\rangle^x - \left\langle\frac{\alpha\lambda}{\Lambda}\right\rangle^x + \left\langle\frac{\alpha}{\Lambda}\right\rangle^x\left\langle\frac{\lambda}{\Lambda}\right\rangle^x\langle\Lambda\rangle^{Hx}.$$

Considering the averaged material coefficients, and stress- and strain-tensor components, relations (4.9) and (4.13) have the same forms as the first and second relations in (2.2) for a point in a smooth medium, and are consistent with the interface boundary conditions.

4.3. Fluid pressure at a planar interface perpendicular to the x axis

For p we may write

$$p = -\alpha^- M^- \varepsilon_{xx}^- - \alpha^- M^- \varepsilon_{zz} - M^- \varepsilon_w^-$$
$$p = -\alpha^+ M^+ \varepsilon_{xx}^+ - \alpha^+ M^+ \varepsilon_{zz} - M^+ \varepsilon_w^+ \qquad (4.14)$$

Before averaging ε_w^- and ε_w^+ we have to express ε_{xx}^- and ε_{xx}^+ using continuous field quantities.

Using (4.7) and expressing ε_w^- and ε_w^+ we obtain

$$\varepsilon_w^- = -\left(\frac{\alpha}{\Lambda}\right)^-\sigma_{xx} - \left(\alpha - \frac{\alpha\lambda}{\Lambda}\right)^-\varepsilon_{zz} - \left(\frac{1}{M} + \frac{\alpha^2}{\Lambda}\right)^- p$$

$$\qquad (4.15)$$

$$\varepsilon_w^+ = -\left(\frac{\alpha}{\Lambda}\right)^+\sigma_{xx} - \left(\alpha - \frac{\alpha\lambda}{\Lambda}\right)^+\varepsilon_{zz} - \left(\frac{1}{M} + \frac{\alpha^2}{\Lambda}\right)^+ p$$

For the arithmetic average of ε_w^- and ε_w^+ we obtain

$$\langle \varepsilon_w \rangle^x = -\left\langle \frac{\alpha}{\Lambda} \right\rangle^x \sigma_{xx} - \left(\langle \alpha \rangle^x - \left\langle \frac{\alpha \lambda}{\Lambda} \right\rangle^x \right) \varepsilon_{zz} - \left\langle \frac{1}{M} + \frac{\alpha^2}{\Lambda} \right\rangle^x p \qquad (4.16)$$

Substituting the r.h.s. of Eq. (4.9) for σ_{xx} eventually leads to the final relation for p at the interface:

$$\begin{aligned}
p = & -\frac{1}{\Psi_x} \left\langle \frac{\alpha}{\Lambda} \right\rangle^x \langle \Lambda \rangle^{Hx} \langle \varepsilon_{xx} \rangle^x \\
& -\frac{1}{\Psi_x} \left(\langle \alpha \rangle^x - \left\langle \frac{\alpha \lambda}{\Lambda} \right\rangle^x + \left\langle \frac{\alpha}{\Lambda} \right\rangle^x \left\langle \frac{\lambda}{\Lambda} \right\rangle^x \langle \Lambda \rangle^{Hx} \right) \varepsilon_{zz} \qquad (4.17) \\
& -\frac{1}{\Psi_x} \langle \varepsilon_w \rangle^x
\end{aligned}$$

where

$$\Psi_x = \left\langle \frac{1}{M} + \frac{\alpha^2}{\Lambda} \right\rangle^x - \left(\left\langle \frac{\alpha}{\Lambda} \right\rangle^x \right)^2 \langle \Lambda \rangle^{Hx} \qquad (4.18)$$

Continuity of ε_{zz} and p, and the arithmetic averaging of the discontinuous ε_w imply the averaged material coefficients $-\frac{1}{\Psi_x} \left\langle \frac{\alpha}{\Lambda} \right\rangle^x \langle \Lambda \rangle^{Hx}$, $-\frac{1}{\Psi_x} \left(\langle \alpha \rangle^x - \left\langle \frac{\alpha \lambda}{\Lambda} \right\rangle^x + \left\langle \frac{\alpha}{\Lambda} \right\rangle^x \left\langle \frac{\lambda}{\Lambda} \right\rangle^x \langle \Lambda \rangle^{Hx} \right)$

and $-\frac{1}{\Psi_x}$. Considering the averaged material coefficients and strain-tensor components, relation (4.17) has the same form as the third relation in (2.2).

Now it is clear why we wrote and used the constitutive equations in the form of (2.2). Without having fluid pressure p explicitly present in relations for σ_{xx} and σ_{zz} we could not average relations for these stress-tensor components, respectively.

4.4. Stress-strain relations for planar interfaces perpendicular to the coordinate axes

We can now express the stress-strain relations for an interface perpendicular to the x axis and for an interface perpendicular to the z axis in a concise form. Define the effective material coefficients

$$A^\xi \equiv \langle \Lambda \rangle^{H\xi}, \quad B^\xi \equiv \left\langle \frac{\lambda}{\Lambda} \right\rangle^\xi A^\xi, \quad C^\xi \equiv \left\langle \frac{\alpha}{\Lambda} \right\rangle^\xi A^\xi$$

$$D^\xi \equiv \langle \Lambda \rangle^\xi - \left\langle \frac{\lambda^2}{\Lambda} \right\rangle^\xi + \left\langle \frac{\lambda}{\Lambda} \right\rangle^\xi B^\xi \tag{4.19}$$

$$E^\xi \equiv \langle \alpha \rangle^\xi - \left\langle \frac{\alpha \lambda}{\Lambda} \right\rangle^\xi - \left\langle \frac{\lambda}{\Lambda} \right\rangle^\xi C^\xi$$

Then the stress-strain relations (4.4), (4.9), (4.13) and (4.17) for the planar interface perpendicular to the x axis may be written as, compare with (2.2),

$$
\begin{aligned}
\sigma_{xx} &= A^x \langle \varepsilon_{xx} \rangle^x + B^x \varepsilon_{zz} - C^x p \\
\langle \sigma_{zz} \rangle^x &= B^x \langle \varepsilon_{xx} \rangle^x + D^x \varepsilon_{zz} - E^x p \\
p &= -\frac{C^x}{\Psi_x} \langle \varepsilon_{xx} \rangle^x - \frac{E^x}{\Psi_x} \varepsilon_{zz} - \frac{1}{\Psi_x} \langle \varepsilon_w \rangle^x \\
\sigma_{xz} &= 2 \langle \mu \rangle^{Hx} \langle \varepsilon_{xz} \rangle^x
\end{aligned}
\tag{4.20}
$$

The corresponding stress-strain relations for the planar interface perpendicular to the z axis are

$$
\begin{aligned}
\langle \sigma_{xx} \rangle^z &= D^z \varepsilon_{xx} + B^z \langle \varepsilon_{zz} \rangle^z - E^z p \\
\sigma_{zz} &= B^z \varepsilon_{xx} + A^z \langle \varepsilon_{zz} \rangle^z - C^z p \\
p &= -\frac{E^z}{\Psi_z} \varepsilon_{xx} - \frac{C^z}{\Psi_z} \langle \varepsilon_{zz} \rangle^z - \frac{1}{\Psi_z} \langle \varepsilon_w \rangle^z \\
\sigma_{xz} &= 2 \langle \mu \rangle^{Hz} \langle \varepsilon_{xz} \rangle^z
\end{aligned}
\tag{4.21}
$$

where

$$\Psi_z = \left\langle \frac{1}{M} + \frac{\alpha^2}{\Lambda} \right\rangle^z - \left(\left\langle \frac{\alpha}{\Lambda} \right\rangle^z \right)^2 \langle \Lambda \rangle^{Hz} \tag{4.22}$$

Recall the matrix form of the constitutive equations (2.1) for a smoothly heterogeneous isotropic poroelastic medium:

$$
\begin{bmatrix} \sigma_{xx} \\ \sigma_{zz} \\ \sigma_{xz} \\ -p \end{bmatrix}
=
\begin{bmatrix}
\Lambda + \alpha^2 M & \lambda + \alpha^2 M & 0 & \alpha M \\
\lambda + \alpha^2 M & \Lambda + \alpha^2 M & 0 & \alpha M \\
0 & 0 & 2\mu & 0 \\
\alpha M & \alpha M & 0 & M
\end{bmatrix}
\begin{bmatrix} \varepsilon_{xx} \\ \varepsilon_{zz} \\ \varepsilon_{xz} \\ \varepsilon_w \end{bmatrix}
$$

We may write relations (4.20) and (4.21) for the interfaces in the same form:

$$
\begin{bmatrix} \sigma_{xx} \\ \langle \sigma_{zz} \rangle^x \\ \sigma_{xz} \\ -p \end{bmatrix} = \begin{bmatrix} A^x + \dfrac{C^x C^x}{\Psi_x} & B^x + \dfrac{C^x E^x}{\Psi_x} & 0 & \dfrac{C^x}{\Psi_x} \\ B^x + \dfrac{C^x E^x}{\Psi_x} & D^x + \dfrac{E^x E^x}{\Psi_x} & 0 & \dfrac{E^x}{\Psi_x} \\ 0 & 0 & 2\langle\mu\rangle^{Hx} & 0 \\ \dfrac{C^x}{\Psi_x} & \dfrac{E^x}{\Psi_x} & 0 & \dfrac{1}{\Psi_x} \end{bmatrix} \begin{bmatrix} \langle \varepsilon_{xx} \rangle^x \\ \varepsilon_{zz} \\ \langle \varepsilon_{xz} \rangle^x \\ \langle \varepsilon_w \rangle^x \end{bmatrix} \tag{4.23}
$$

$$
\begin{bmatrix} \langle \sigma_{xx} \rangle^z \\ \sigma_{zz} \\ \sigma_{xz} \\ -p \end{bmatrix} = \begin{bmatrix} D^z + \dfrac{E^z E^z}{\Psi_z} & B^z + \dfrac{C^z E^z}{\Psi_z} & 0 & \dfrac{E^z}{\Psi_z} \\ B^z + \dfrac{C^z E^z}{\Psi_z} & A^z + \dfrac{C^z C^z}{\Psi_z} & 0 & \dfrac{C^z}{\Psi_z} \\ 0 & 0 & 2\langle\mu\rangle^{Hz} & 0 \\ \dfrac{E^z}{\Psi_z} & \dfrac{C^z}{\Psi_z} & 0 & \dfrac{1}{\Psi_z} \end{bmatrix} \begin{bmatrix} \varepsilon_{xx} \\ \langle \varepsilon_{zz} \rangle^z \\ \langle \varepsilon_{xz} \rangle^z \\ \langle \varepsilon_w \rangle^z \end{bmatrix} \tag{4.24}
$$

The stiffness matrices in relations (2.1), (4.23) and (4.24) have the same form and the same number of 7 (considering the matrix symmetry) non-zero elements. The difference is in the number of independent elements. The matrix in (2.1) has 4 independent elements whereas the matrices in relations (4.23) and (4.24) have all 7 elements independent.

4.5. Note on a nonplanar interface

A nonplanar smooth surface may be locally approximated by a planar interface tangential to the surface at a given point. The stiffness matrix for a planar interface in a general orientation has all 10 (considering the matrix symmetry) elements non-zero though obviously only 7 independent. This means that all strain-tensor components are necessary for calculating each stress-tensor component at a point of the interface. This is a considerable increase either in memory requirement or computing time. In 3D the increase would be more dramatic.

As in the case of the discrete representation of the material interface between elastic media (Moczo et al. 2002 and 2014, Kristek et al. 2017) instead of treating explicitly a nonplanar interfaces by locally tangential planar interfaces, we decide for an approximate averaging in a grid cell.

4.6. Averaging in the grid cell

We make the following decision on averaging the medium:

1. The stiffness matrix of the averaged medium will have the same structure as matrix (2.1) except that the number of independent elements may be different.

2. If a grid cell contains a planar interface (between two homogeneous materials) perpendicular to the x axis, the stiffness matrix of the averaged medium in the cell will be that of relation (4.23) and, consequently, the stress-strain relation at the interface may be written in the form (4.20). If a grid cell contains a planar interface (between two homogeneous materials) perpendicular to the z axis, the stiffness matrix of the averaged medium in the cell will be that of relation (4.24) and, consequently, the stress-strain relation at the interface may be written in the form (4.21).

Let us write relations (4.20) and (4.21) in a joint general form:

$$
\begin{aligned}
\sigma_{xx} &= XX\ \varepsilon_{xx} + XZ\ \varepsilon_{zz} - XP\ p \\
\sigma_{zz} &= XZ\ \varepsilon_{xx} + ZZ\ \varepsilon_{zz} - ZP\ p \\
p &= -\frac{XP}{\Psi}\ \varepsilon_{xx} - \frac{ZP}{\Psi}\ \varepsilon_{zz} - \frac{1}{\Psi}\ \varepsilon_w \\
\sigma_{xz} &= 2\left\langle \mu \right\rangle^{Hz} \varepsilon_{xz}
\end{aligned}
\tag{4.25}
$$

Here we do not indicate averaging of the stress- and strain-tensor components. The two above requirements on averaging in the grid cell are met by the following averages:

$$
XX = \left\langle \left\langle \Lambda - \frac{\lambda^2}{\Lambda} \right\rangle^z + \left(\left\langle \frac{\lambda}{\Lambda} \right\rangle^z \right)^2 \left\langle \Lambda \right\rangle^{Hz} \right\rangle^{Hx}
$$

$$
ZZ = \left\langle \left\langle \Lambda - \frac{\lambda^2}{\Lambda} \right\rangle^x + \left(\left\langle \frac{\lambda}{\Lambda} \right\rangle^x \right)^2 \left\langle \Lambda \right\rangle^{Hx} \right\rangle^{Hz}
\tag{4.26}
$$

$$
XZ = \left\langle \frac{\lambda}{\Lambda} \right\rangle^{xz} \left\langle \Lambda \right\rangle^{Hxz}
$$

$$
XP = \left\langle \left\langle \Lambda - \frac{\alpha\lambda}{\Lambda} \right\rangle^z + \left\langle \frac{\alpha}{\Lambda} \right\rangle^z \left\langle \frac{\lambda}{\Lambda} \right\rangle^z \left\langle \Lambda \right\rangle^{Hz} \right\rangle^{Hx}
$$

$$
\left\langle \frac{\left\langle \alpha - \frac{\alpha\lambda}{\Lambda} \right\rangle^z + \left\langle \frac{\alpha}{\Lambda} \right\rangle^z \left\langle \frac{\lambda}{\Lambda} \right\rangle^z \left\langle \Lambda \right\rangle^{Hz}}{\left\langle \Lambda - \frac{\alpha\lambda}{\Lambda} \right\rangle^z + \left\langle \frac{\alpha}{\Lambda} \right\rangle^z \left\langle \frac{\lambda}{\Lambda} \right\rangle^z \left\langle \Lambda \right\rangle^{Hz}} \right\rangle^x
\tag{4.27}
$$

$$ZP = \left\langle \frac{\left\langle \left\langle \Lambda - \dfrac{\alpha\lambda}{\Lambda} \right\rangle^{x} + \left\langle \dfrac{\alpha}{\Lambda} \right\rangle^{x} \left\langle \dfrac{\lambda}{\Lambda} \right\rangle^{x} \langle \Lambda \rangle^{Hx} \right\rangle^{Hz}}{} \right.$$

$$\left. \frac{\left\langle \left\langle \alpha - \dfrac{\alpha\lambda}{\Lambda} \right\rangle^{x} + \left\langle \dfrac{\alpha}{\Lambda} \right\rangle^{x} \left\langle \dfrac{\lambda}{\Lambda} \right\rangle^{x} \langle \Lambda \rangle^{Hx} \right\rangle}{\left\langle \Lambda - \dfrac{\alpha\lambda}{\Lambda} \right\rangle^{x} + \left\langle \dfrac{\alpha}{\Lambda} \right\rangle^{x} \left\langle \dfrac{\lambda}{\Lambda} \right\rangle^{x} \langle \Lambda \rangle^{Hx}} \right\rangle^{z} \tag{4.28}$$

$$\Psi = \left\langle \frac{1}{M} + \frac{\alpha^{2}}{\Lambda} \right\rangle^{xz} - \left(\left\langle \frac{\alpha}{\Lambda} \right\rangle^{xz} \right)^{2} \langle \Lambda \rangle^{Hxz} \tag{4.29}$$

The constitutive relation for the averaged medium in the grid cell may be written in the form of the constitutive relation for a smoothly heterogeneous medium (2.1):

$$
\begin{bmatrix} \sigma_{xx} \\ \sigma_{zz} \\ \sigma_{xz} \\ -p \end{bmatrix} =
\begin{bmatrix}
XX + \dfrac{XP\,XP}{\Psi} & XZ + \dfrac{XP\,ZP}{\Psi} & 0 & \dfrac{XP}{\Psi} \\
XZ + \dfrac{XP\,ZP}{\Psi} & ZZ + \dfrac{ZP\,ZP}{\Psi} & 0 & \dfrac{ZP}{\Psi} \\
0 & 0 & 2\langle \mu \rangle^{Hx} & 0 \\
\dfrac{XP}{\Psi} & \dfrac{ZP}{\Psi} & 0 & \dfrac{1}{\Psi}
\end{bmatrix}
\begin{bmatrix} \varepsilon_{xx} \\ \varepsilon_{zz} \\ \varepsilon_{xz} \\ \varepsilon_{w} \end{bmatrix} \tag{4.30}
$$

The stiffness matrices in relations (2.1) and (4.30) have the same number of 7 (considering the matrix symmetry) non-zero elements. The difference is in the number of independent elements. The matrix in (2.1) has 4 independent elements whereas the matrix in (4.30) has all 7 independent elements. Let us recall that the stiffness matrices in relations (4.23) and (4.24) for the planar interface perpendicular to the x and z axis, respectively, also have 7 independent elements. This is due to the two-dimensionality of the considered problem.

Note that the averaged stiffness matrix represents an orthorhombic medium. The structure of the matrix is the most natural choice for the staggered-grid scheme. The number of algebraic operations for updating stress tensor and fluid pressure is unchanged compared to the homogeneous or smoothly heterogeneous medium. Additional non-zero elements in the stiffness matrix would require a more complicated scheme.

Note also that each average coefficient applies to an area of the grid cell $h \times h$ centred at a position of the corresponding stress-tensor component or fluid pressure. In case of a generally heterogeneous medium it is to be evaluated by a numerical integration.

5 EQUATIONS OF MOTION

The equations of motion may be written as

$$
\begin{aligned}
\rho\, \dot{v}_x &= \sigma_{xx},_x + \sigma_{xz},_z - \rho_f\, \dot{q}_x \\
\rho\, \dot{v}_z &= \sigma_{xz},_x + \sigma_{zz},_z - \rho_f\, \dot{q}_z \\
m\, \dot{q}_x &= -p,_x - \rho_f\, \dot{v}_x - b\, q_x \\
m\, \dot{q}_z &= -p,_z - \rho_f\, \dot{v}_z - b\, q_z
\end{aligned}
\tag{5.1}
$$

where v_x and v_z are solid particle velocities, q_x and q_z are fluid particle velocities relative to the solid, dot above a symbol indicates temporal derivative, $\rho = (1-\phi)\rho_s + \phi\rho_f$ is the composite (or total) density, ρ_s and ρ_f are the solid and fluid densities, respectively, $m = T\rho_f/\phi$ is the mass coupling coefficient and T is tortuosity, $b = \eta/\kappa$ is the resistive damping (friction), η is the dynamic viscosity of fluid and κ is the permeability.

5.1. Averaging at a planar interface perpendicular to the x axis

For the two halfspaces in a contact we may write equations for $\dot{v}_x$ and $\dot{q}_x$ as

$$
\begin{aligned}
\rho^-\, \dot{v}_x &= \sigma_{xx}^-,_x + \sigma_{xz}^-,_z - \rho_f^-\, \dot{q}_x \\
\rho^+\, \dot{v}_x &= \sigma_{xx}^+,_x + \sigma_{xz}^+,_z - \rho_f^+\, \dot{q}_x
\end{aligned}
\tag{5.2}
$$

and

$$
\begin{aligned}
m^-\, \dot{q}_x &= -p,_x^- - \rho_f^-\, \dot{v}_x - b^-\, q_x \\
m^+\, \dot{q}_x &= -p,_x^+ - \rho_f^+\, \dot{v}_x - b^+\, q_x
\end{aligned}
\tag{5.3}
$$

The averaging of Eqs. (5.2) and (5.3) gives, respectively,

$$
\langle\rho\rangle^x\, \dot{v}_x = \langle\sigma_{xx},_x + \sigma_{xz},_z\rangle^x - \langle\rho_f\rangle^x\, \dot{q}_x
\tag{5.4}
$$

and

$$
\langle m\rangle^x\, \dot{q}_x = -\langle p,_x\rangle^x - \langle\rho_f\rangle^x\, \dot{v}_x - \langle b\rangle^x\, q_x
\tag{5.5}
$$

Eliminating $\dot{q}_x$ and $\dot{v}_x$ from Eqs. (5.4) and (5.5), respectively, gives

$$
\left(\frac{\langle\rho\rangle^x}{\langle\rho_f\rangle^x} - \frac{\langle\rho_f\rangle^x}{\langle m\rangle^x}\right)\dot{v}_x = \frac{1}{\langle\rho_f\rangle^x}\langle\sigma_{xx},_x + \sigma_{xz},_z\rangle^x + \frac{1}{\langle m\rangle^x}\langle p,_x\rangle^x + \frac{\langle b\rangle^x}{\langle m\rangle^x}q_x
\tag{5.6}
$$

and

$$\left(\frac{\langle\rho\rangle^x}{\langle\rho_f\rangle^x} - \frac{\langle\rho_f\rangle^x}{\langle m\rangle^x} \right)\dot{q}_x = -\frac{1}{\langle m\rangle^x}\langle\sigma_{xx},_x + \sigma_{xz},_z\rangle^x - \frac{\langle\rho\rangle^x}{\langle\rho_f\rangle^x}\frac{1}{\langle m\rangle^x}\langle p,_x\rangle^x - \frac{\langle\rho\rangle^x}{\langle\rho_f\rangle^x}\frac{\langle b\rangle^x}{\langle m\rangle^x}q_x \quad (5.7)$$

Equations for $\dot{v}_z$ and $\dot{q}_z$ may be written as

$$
\begin{aligned}
\rho^- \dot{v}_z &= \sigma_{zx}^-,_x + \sigma_{zz}^-,_z - \rho_f^- \dot{q}_z^- \\
\rho^+ \dot{v}_z &= \sigma_{zx}^+,_x + \sigma_{zz}^+,_z - \rho_f^+ \dot{q}_z^+
\end{aligned}
\quad (5.8)
$$

and

$$
\begin{aligned}
m^- \dot{q}_z^- &= -p,_z^- - \rho_f^- \dot{v}_z - b^- q_z^- \\
m^+ \dot{q}_z^+ &= -p,_z^+ - \rho_f^+ \dot{v}_z - b^+ q_z^+
\end{aligned}
\quad (5.9)
$$

The averaging of Eqs. (5.8) and (5.9) gives, respectively

$$\left\langle \frac{\rho}{\rho_f} \right\rangle^x \dot{v}_z = \left\langle \frac{1}{\rho_f}\left(\sigma_{zx},_x + \sigma_{zz},_z\right) \right\rangle^x - \langle\dot{q}_z\rangle^x \quad (5.10)$$

and

$$\langle\dot{q}_z\rangle^x = -\left\langle \frac{1}{m}p,_z \right\rangle^x - \left\langle \frac{\rho_f}{m} \right\rangle^x \dot{v}_z - \left\langle \frac{b}{m}q_z \right\rangle^x \quad (5.11)$$

Eliminating $\dot{q}_x$ and $\dot{v}_x$ from Eqs. (5.10) and (5.11), respectively, gives

$$\left(\left\langle \frac{\rho}{\rho_f} \right\rangle^x - \left\langle \frac{\rho_f}{m} \right\rangle^x \right)\dot{v}_z = \left\langle \frac{1}{\rho_f}\left(\sigma_{zx},_x + \sigma_{zz},_z\right) \right\rangle^x + \left\langle \frac{1}{m}p,_z \right\rangle^x + \left\langle \frac{b}{m}q_z \right\rangle^x \quad (5.12)$$

and

$$\left(\left\langle \frac{\rho}{\rho_f} \right\rangle^x - \left\langle \frac{\rho_f}{m} \right\rangle^x \right)\langle\dot{q}_z\rangle^x =$$
$$- \left\langle \frac{\rho_f}{m} \right\rangle^x \left\langle \frac{1}{\rho_f}\left(\sigma_{zx},_x + \sigma_{zz},_z\right) \right\rangle^x - \left\langle \frac{\rho}{\rho_f} \right\rangle^x \left\langle \frac{1}{m}p,_z \right\rangle^x - \left\langle \frac{\rho}{\rho_f} \right\rangle^x \left\langle \frac{b}{m}q_z \right\rangle^x \quad (5.13)$$

5.2. Equations of motion for the averaged medium

The equations of motion can be written in a matrix form

$$\begin{bmatrix} \dot{v}_x \\ -\dot{q}_x \\ \dot{v}_z \\ -\dot{q}_z \end{bmatrix} = \mathbf{M}(x,z) \begin{bmatrix} \sigma_{xx},_x + \sigma_{xz},_z \\ p,_x \\ q_x \\ \sigma_{zz},_z + \sigma_{xz},_x \\ p,_z \\ q_z \end{bmatrix} \quad (5.14)$$

We are neglecting here the averaging of the field quantities. Define auxiliary quantities

$$F^{\xi} \equiv \frac{1}{\left\langle \rho_f \right\rangle^{\xi}} \qquad G^{\xi} \equiv \frac{1}{\left\langle m \right\rangle^{\xi}} \qquad H^{\xi} \equiv \frac{\left\langle b \right\rangle^{\xi}}{\left\langle m \right\rangle^{\xi}}$$

$$P^{\xi} \equiv \frac{\left\langle \rho \right\rangle^{\xi}}{\left\langle \rho_f \right\rangle^{\xi}} \qquad Q^{\xi} \equiv \frac{\left\langle \rho_f \right\rangle^{\xi}}{\left\langle m \right\rangle^{\xi}} \qquad R^{\xi} \equiv \left\langle \frac{1}{\rho_f} \right\rangle^{\xi} \qquad (5.15)$$

$$S^{\xi} \equiv \left\langle P^{\xi} \right\rangle - \left\langle Q^{\xi} \right\rangle$$

Then, in analogy with relation (4.30) for the constitutive relation for the averaged medium, we may write matrix $\mathbf{M}(x,z)$ for the averaged medium in the form

$$\mathbf{M}(x,z) =$$

$$\begin{bmatrix} \dfrac{\left\langle F^x \right\rangle^z}{\left\langle S^x \right\rangle^z} & \dfrac{\left\langle G^x \right\rangle^z}{\left\langle S^x \right\rangle^z} & \dfrac{\left\langle H^x \right\rangle^z}{\left\langle S^x \right\rangle^z} & 0 & 0 & 0 \\[3mm] \dfrac{\left\langle R^x \right\rangle^z \left\langle \frac{G^x}{R^x} \right\rangle^z}{\left\langle S^x \right\rangle^z} & \dfrac{\left\langle P^x \right\rangle^z \left\langle G^x \right\rangle^z}{\left\langle S^x \right\rangle^z} & \dfrac{\left\langle P^x \right\rangle^z \left\langle H^x \right\rangle^z}{\left\langle S^x \right\rangle^z} & 0 & 0 & 0 \\[3mm] 0 & 0 & 0 & \dfrac{\left\langle F^z \right\rangle^x}{\left\langle S^z \right\rangle^x} & \dfrac{\left\langle G^z \right\rangle^x}{\left\langle S^z \right\rangle^x} & \dfrac{\left\langle H^z \right\rangle^x}{\left\langle S^z \right\rangle^x} \\[3mm] 0 & 0 & 0 & \dfrac{\left\langle R^z \right\rangle^x \left\langle \frac{G^z}{R^z} \right\rangle^x}{\left\langle S^z \right\rangle^x} & \dfrac{\left\langle P^z \right\rangle^x \left\langle G^z \right\rangle^x}{\left\langle S^z \right\rangle^x} & \dfrac{\left\langle P^z \right\rangle^x \left\langle H^z \right\rangle^x}{\left\langle S^z \right\rangle^x} \end{bmatrix} \quad (5.16)$$

Note that each averaged coefficient applies to an area of the grid cell $h \times h$ centred at a position of the corresponding particle-velocity component. In case of a generally heterogeneous medium it is to be evaluated by a numerical integration.

6 THE FINITE-DIFFERENCE SCHEME

Denote the discrete grid values of the particle-velocity v_x, v_z and q_x, q_z by VX, VZ and QX, QZ, respectively. Similarly denote the stress-tensor components $\sigma_{xx}, \sigma_{zz}, \sigma_{xz}$ and fluid pressure p by TXX, TZZ, TXZ and P, respectively. For the grid values of the material parameters we will use symbols defined by Eqs. (4.26) – (4.29) and (5.15). Fig. 1 shows

positions of the field quantities and material parameters in the grid cell. (Note that we indicate material parameters as they appear in the equations for the smoothly heterogeneous medium because showing the averaged parameters would require unreasonably large and complicated figure.) We may approximate equations of motion (5.14) and constitutive equations (4.30) at the time levels n and $n-1/2$, respectively. Define discrete operators of the 4th-order approximation of the 1st spatial derivative with respect to $x-$ and $z-$ axes, respectively:

$$
\begin{aligned}
D_x^{(4)} \Phi_{I,L}^n &\equiv \frac{1}{h} \left[\frac{9}{8} \left(\Phi_{I+1/2,L}^n - \Phi_{I-1/2,L}^n \right) - \frac{1}{24} \left(\Phi_{I+3/2,L}^n - \Phi_{I-3/2,L}^n \right) \right] \\
D_z^{(4)} \Phi_{I,L}^n &\equiv \frac{1}{h} \left[\frac{9}{8} \left(\Phi_{I,L+1/2}^n - \Phi_{I,L-1/2}^n \right) - \frac{1}{24} \left(\Phi_{I,L+3/2}^n - \Phi_{I,L-3/2}^n \right) \right]
\end{aligned}
\tag{5.17}
$$

Here we present the FD schemes for v_x and q_x at the spatial grid position $I, L+1/2$, and for p and σ_{xx} at $I+1/2, L+1/2$. The schemes are

$$
\begin{aligned}
VX_{I,L+1/2}^{n+1/2} = \; & VX_{I,L+1/2}^{n-1/2} + \frac{1}{\left\langle S^x \right\rangle_{I,L+1/2}^z} \frac{\Delta}{h} \\
& \left\{ \left\langle F^x \right\rangle_{I,L+1/2}^z \left[D_x^{(4)} TXX_{I,L+1/2}^n + D_z^{(4)} TXZ_{I,L+1/2}^n \right] \right. \\
& + \left\langle G^x \right\rangle_{I,L+1/2}^z D_x^{(4)} P_{I,L+1/2}^n \\
& \left. + \left\langle H^x \right\rangle_{I,L+1/2}^z \left[\frac{h}{2} \left(QX_{I,L+1/2}^{n+1/2} + QX_{I,L+1/2}^{n-1/2} \right) \right] \right\}
\end{aligned}
\tag{5.18}
$$

$$
\begin{aligned}
QX_{I,L+1/2}^{n+1/2} = \; & \left(\frac{\left\langle S^x \right\rangle^z - \frac{\Delta}{2} \left\langle P^x \right\rangle^z \left\langle H^x \right\rangle^z}{\left\langle S^x \right\rangle^z + \frac{\Delta}{2} \left\langle P^x \right\rangle^z \left\langle H^x \right\rangle^z} \right)_{I,L+1/2} QX_{I,L+1/2}^{n-1/2} - \\
& - \frac{1}{\left(\left\langle S^x \right\rangle^z + \frac{\Delta}{2} \left\langle P^x \right\rangle^z \left\langle H^x \right\rangle^z \right)_{I,L+1/2}} \frac{\Delta}{h} \\
& \left\{ \left(\left\langle R^x \right\rangle^z \left\langle \frac{G^x}{R^x} \right\rangle^z \right)_{I,L+1/2} \left[D_x^{(4)} TXX_{I,L+1/2}^n + D_z^{(4)} TXZ_{I,L+1/2}^n \right] \right. \\
& \left. + \left(\left\langle P^x \right\rangle^z \left\langle G^x \right\rangle^z \right)_{I,L+1/2} D_x^{(4)} P_{I,L+1/2}^n \right\}
\end{aligned}
\tag{5.19}
$$

$$TXX^n_{I+1/2,L+1/2} = TXX^{n-1}_{I+1/2,L+1/2}$$

$$+ \frac{\Delta}{h}\left\{\left(XX + \frac{XP^2}{\Psi}\right)_{I+1/2,L+1/2} D^{(4)}_x VX^{n-1/2}_{I+1/2,L+1/2}\right.$$

$$+ \left(XZ + \frac{XP\,ZP}{\Psi}\right)_{I+1/2,L+1/2} D^{(4)}_z VZ^{n-1/2}_{I+1/2,L+1/2}$$

$$- \left.\left(\frac{XP}{\Psi}\right)_{I+1/2,L+1/2}\left[D^{(4)}_x QX^{n-1/2}_{I+1/2,L+1/2} + D^{(4)}_z QZ^{n-1/2}_{I+1/2,L+1/2}\right]\right\} \qquad (5.20)$$

$$P^n_{I+1/2,L+1/2} = P^{n-1}_{I+1/2,L+1/2}$$

$$+ \frac{\Delta}{h}\left\{\left(\frac{XP}{\Psi}\right)_{I+1/2,L+1/2} D^{(4)}_x VX^{n-1/2}_{I+1/2,L+1/2}\right.$$

$$+ \left(\frac{ZP}{\Psi}\right)_{I+1/2,L+1/2} D^{(4)}_z VZ^{n-1/2}_{I+1/2,L+1/2}$$

$$- \left.\left(\frac{1}{\Psi}\right)_{I+1/2,L+1/2}\left[D^{(4)}_x QX^{n-1/2}_{I+1/2,L+1/2} + D^{(4)}_z QZ^{n-1/2}_{I+1/2,L+1/2}\right]\right\} \qquad (5.21)$$

Figure 1. Positions of the field quantities (discrete approximations of the true quantities in the continuum) and material parameters. For simplicity we indicate the material parameters as they appear in the equations for the smoothly heterogeneous medium. The averaged parameters entering the FD scheme would require too much space in the figure.

The FD schemes are computationally efficient if the resistive damping (friction) $b = 0$. If the resistive damping is non-zero, the schemes require very small time step and thus become computationally inefficient. To avoid this, we can partition each of Eqs. (5.4), (5.5), (5.12) and (5.13) into stiff and non-stiff equation as suggested by Carcione & Quiroga-Goode (1995). The corresponding FD schemes are given in Appendix.

7 NUMERICAL VERIFICATION

Because the developed discrete representation is approximate, it is necessary to test it numerically by comparing the finite-difference (FD) seismograms with seismograms obtained using independent verified methods. First we will restrict the numerical tests to the case with zero resistive damping, that is, with $b = 0$. We want to stress that a non-zero value would just considerably attenuate the slow P wave and consequently mask a potential inaccuracy in the discrete representation of the interface. Eventually we will consider a test for a non-zero resistive damping.

7.1. Two halfspaces with a planar interface parallel with a grid plane – comparison with an exact solution

The discrete representation of the material interface between two elastic and viscoelastic materials (Moczo et al. 2002, 2014, Kristek & Moczo 2003, Kristek et al. 2017) is capable to "sense" an arbitrary position of the interface in-between two grid points. Here we present a series of numerical tests demonstrating that the developed representation of the interface between two poroelastic materials has the same capability.

Fig. 2 shows horizontal interface of two poroelastic halfspaces, positions of receivers and the point of intersection of the computational plane with a perpendicular line source generating only compressional waves. The source is applied to both solid and fluid phases. Fig. 3 shows the source-time function. Table 1 lists material parameters. We chose large values of the fast P-wave velocities in the halfspaces and a large value of the velocity contrast at the interface in order to enhance potential inaccuracy of the developed representation. The large velocities also make it possible to see differences due to different positions of the interface within one grid cell. Considering the effective maximum source frequency 5Hz, the corresponding minimum wavelength is 151m. The time step is 0.0011s and spatial grid spacing is 14m. We chose this grid spacing in order to safely avoid a grid dispersion of the slow P wave which is not attenuated in the case of the poroelastic medium (medium with zero resistive damping b). Fig. 4 shows 5 positions of the horizontal planar interface in the grid. The source and receivers are at the same positions in the grid in all 5 cases. Fig. 5a shows the horizontal component of the particle velocity v_x at receiver R_T for all 5 positions of the interface. The black-line FD seismograms are compared with the red-line exact seismograms calculated using the code Gar6more2D developed by Diaz & Ezziani (2008). The bottom right panel compares the 5 FD seismograms in order to illustrate the differences due to different positions of the interface with respect to the grid, source and receiver. Fig. 5b shows the same but for receiver R_R. It is clear from both figures that the FD

seismograms are in very good agreement with the exact seismograms. In order to further demonstrate the sensitivity of the developed representation, we performed additional tests. They are indicated in Fig. 6. Again for the fixed positions of the source and receivers in the grid, we conside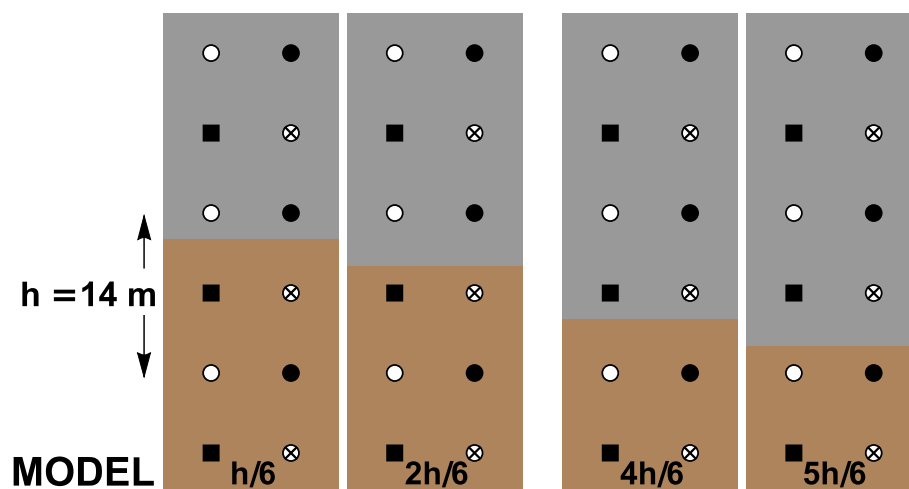r 4 different positions of the interface: taking the A position (Fig. 4) as a reference, the 4 positions are at distances $h/6$, $2h/6$, $4h/6$ and $5h/6$, h meaning the grid spacing, downward from the A position. This means that we have two couples of positions with the distance between two positions in each couple just $h/6$. The left panel of Fig. 7 compares the exact seismograms themselves in order to show the small difference due to positions, whereas the right panel compares the FD seismograms with the exact seismograms. The comparison confirms the remarkable accuracy/sensitivity of the discrete representation.

		upper halfspace	lower halfspace
Solid	Bulk modulus, $K_s (GPa)$	80.0	5.2
	Density, $\rho_s (kg\,m^{-3})$	2500	2250
Matrix	Bulk modulus, $K_m (GPa)$	37.0	2.2
	Shear modulus, $\mu (GPa)$	26.1	2.4
	Porosity, ϕ	0.5	0.25
	Tortuosity, T	2.0	2.0
Fluid	Density, $\rho_f (kg\,m^{-3})$	1040	1040
	Viscosity, $\eta (Pas)$	0.0	0.0
	Bulk modulus, $K_f (GPa)$	2.5	2.5
Velocity	Fast P-wave $(m\,s^{-1})$	6916	1956
	Slow P-wave $(m\,s^{-1})$	1092	757
	S-wave $(m\,s^{-1})$	4157	1149

Table 1. Material parameters describing the model consisting of two homogeneous poroelastic halfspaces.
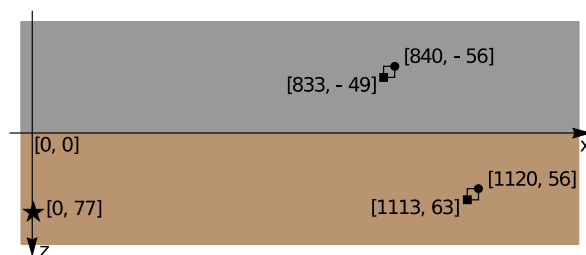
Figure 2. Schematic presentation of the configuration A with the horizontal interface between two poroelastic halfspaces. Position of the point of intersection of the computational plane with a perpendicular line source generating only compressional waves is indicated by a star. Positions of the receivers for the v_x and v_z solid particle-velocity components are indicated by solid squares and circles, respectively (their positions differ due to the staggered grid). The depicted coordinate system serves only for simple indication of relative positions of the source, receivers and interface.
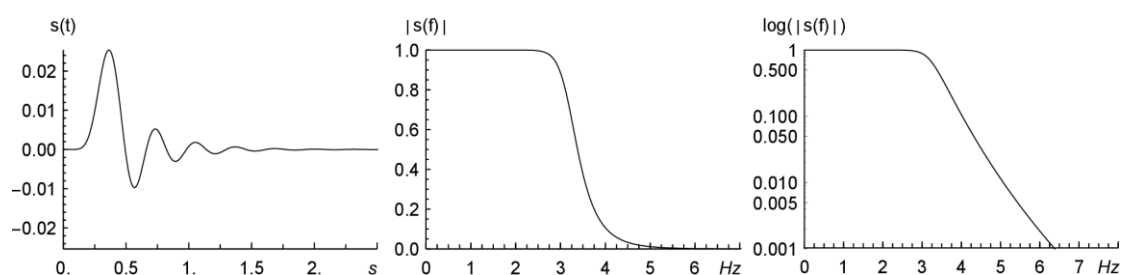
Figure 3. Source time function, and its amplitude and log Fourier spectra.
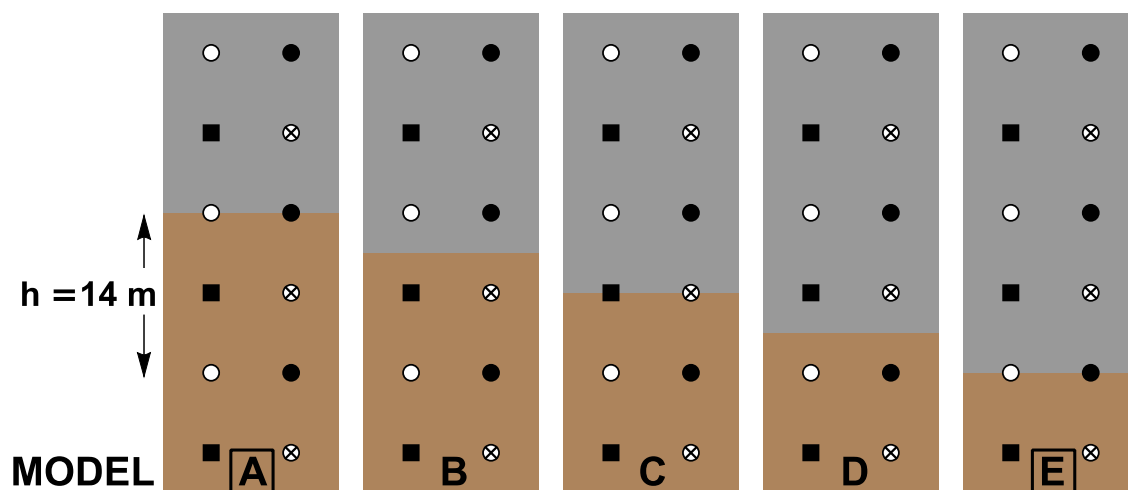
Figure 4. 5 positions of the horizontal planar interface in the grid labelled A, B, C, D and E. Labels A and E are framed in order to indicate that the distance between the two positions is just one grid spacing. The source and receivers are at the same positions in the grid in all 5 cases.
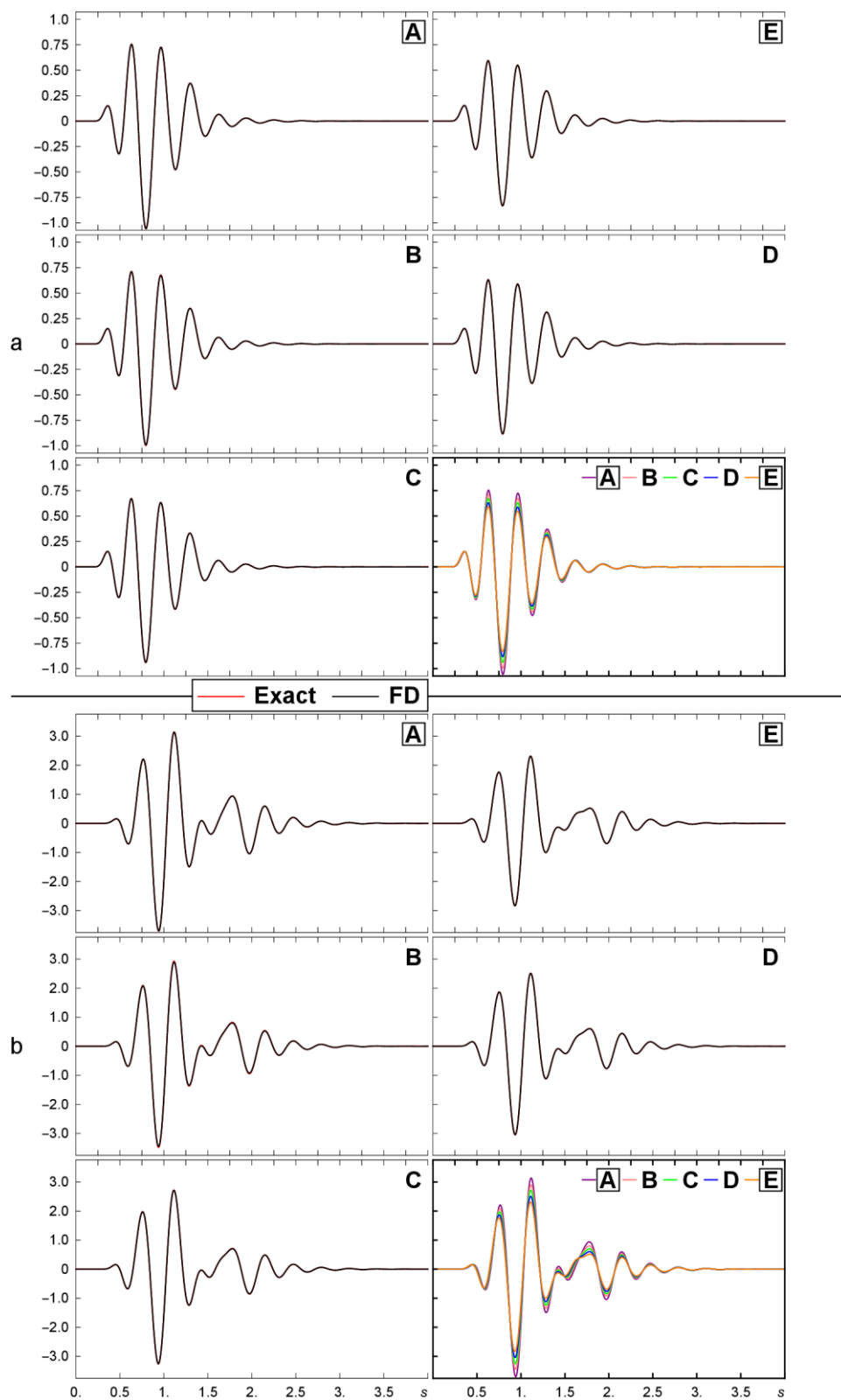
Figure 5. Illustration of accuracy of the developed discrete representation: comparison of the horizontal component of the solid particle velocity v_x calculated by our FD scheme and the exact method by Diaz & Ezziani (2008). Labels A – E indicate the 5 different positions of the horizontal interface in the grid shown in Fig. 5. The upper panel labelled a is for receiver R_T, the lower panel labelled b is for receiver R_R. In each of the two panels, the lower right frame labelled A B C D E shows FD seismograms for all 5 positions in order to illustrate the scatter in seismograms due to different positions of the interface.

Figure 6. 4 different positions of the interface. Considering position A (Fig. 5) as a reference, the 4 positions are at distances $h/6$, $2h/6$, $4h/6$ and $5h/6$, h meaning the grid spacing, downward from A position. The source and receivers are at the same positions in the grid in all 4 cases.
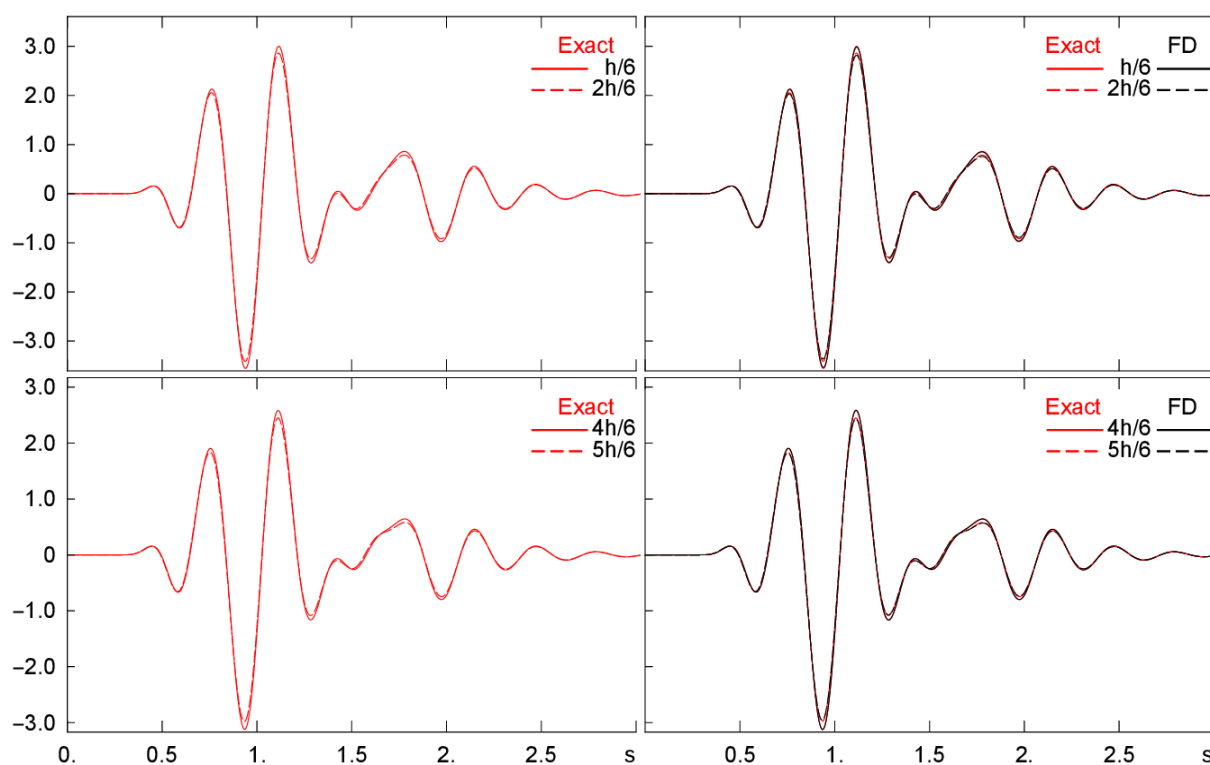
Figure 7. Illustration of sensitivity of the developed discrete representation: comparison of the horizontal component of the solid particle velocity for two couples of positions of the interface in the grid shown in Fig. 6. The distance between two positions is just $1/6$ of the grid spacing h. The left panel shows only exact seismograms in order to visualize the small difference between the seismograms. The right panel shows both the exact and FD seismograms. The FD scheme is capable of sensing the small difference in position of the interface in the grid.

7.2. Two halfspaces with a planar interface in an oblique position with respect to the spatial grid – comparison with an exact solution

Here we demonstrate the capability of the discrete representation to "sense" an oblique position of the interface in the grid. We consider the same poroelastic materials in planar contact and the same type of the source as in the previous section. Fig. 8 shows 5 different orientations of the interface with respect to the horizontal grid line: $5°$, $15°$, $25°$, $35°$ and $45°$. We consider two positions of the interface for the $45°$ angle – one with the interface coinciding with the cell diagonal and one shifted a little bit from the diagonal. Fig. 9 compares the FD seismograms with the exact seismograms calculated with the Gar6more2D code (Diaz & Ezziani 2008). As in the case of the arbitrary position of the horizontal interface with respect to the spatial grid it is obvious that the discrete representation can sufficiently accurately model an oblique position of the interface in the grid.
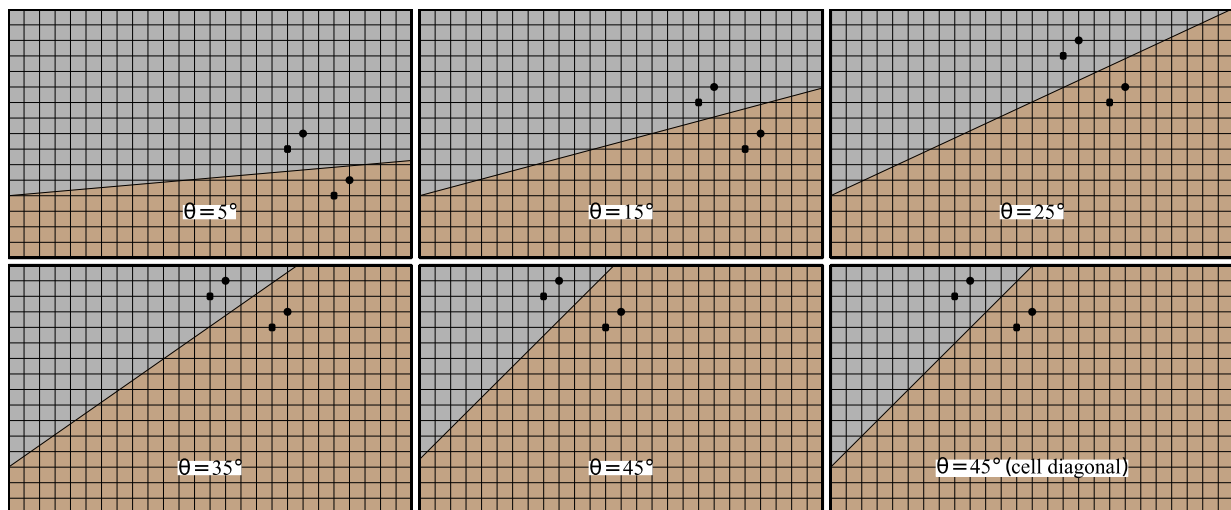
Figure 8. 5 positions of the horizontal interface in the grid differing in the angle between the interface and horizontal grid line.
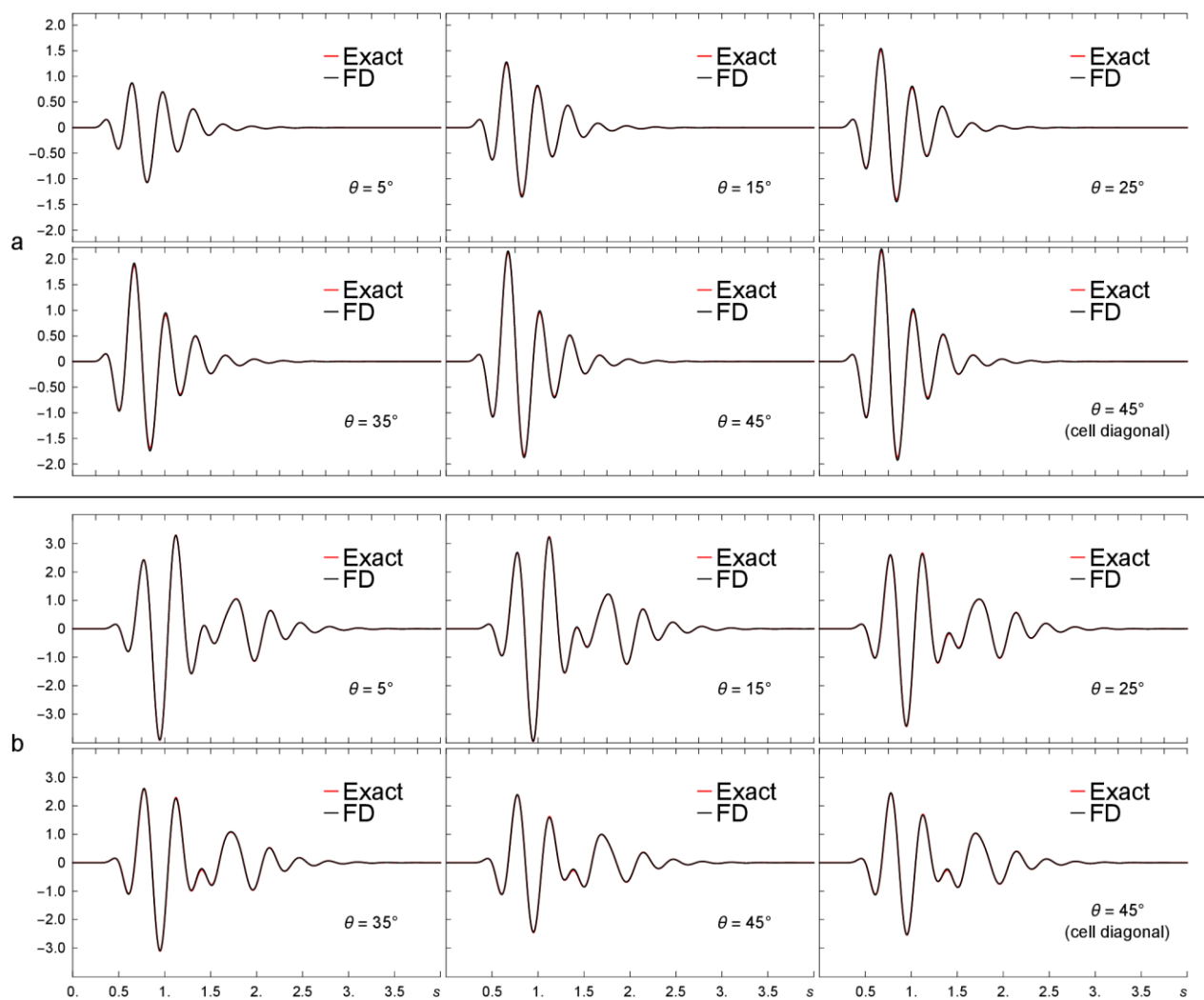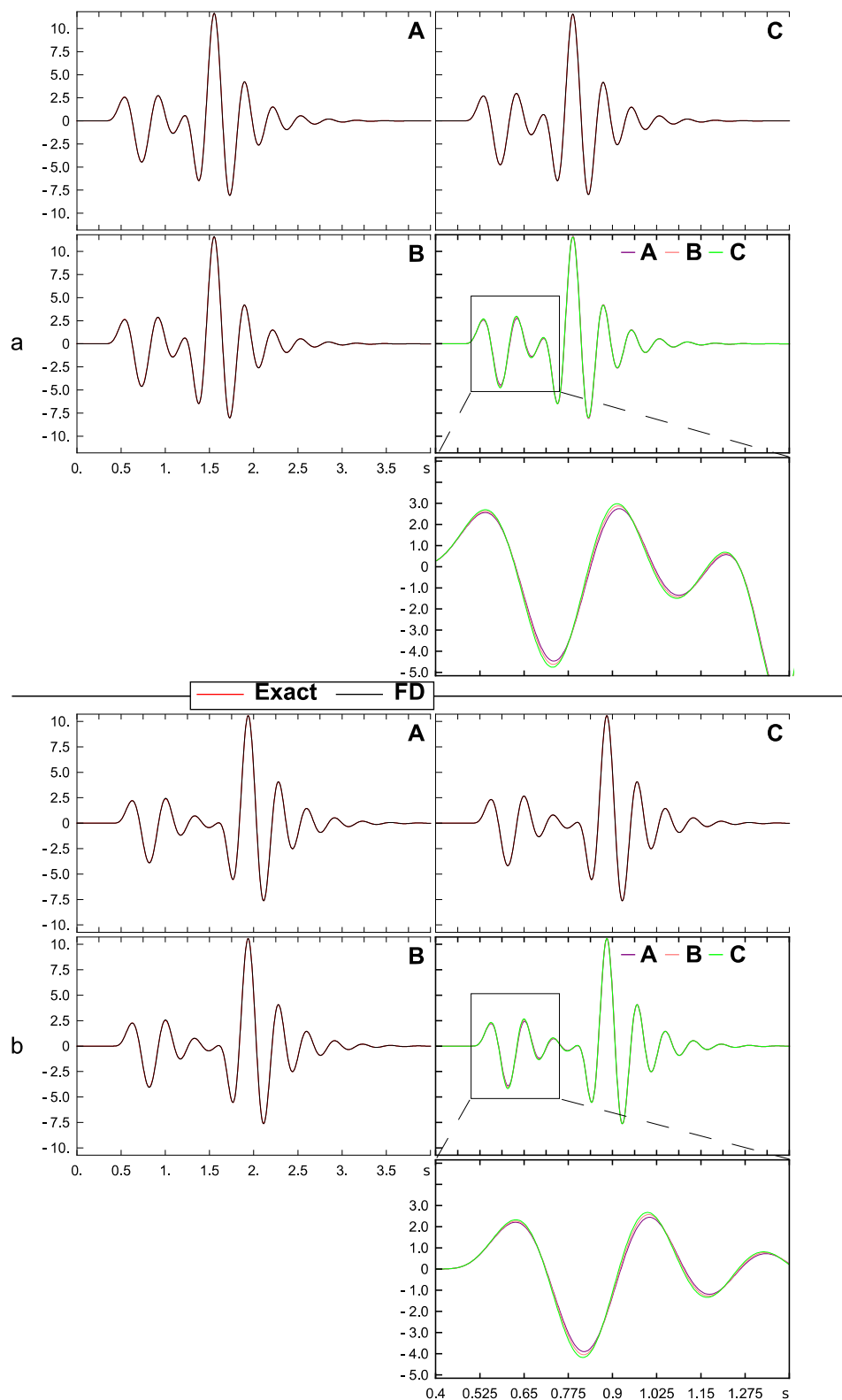
Figure 9. Illustration of accuracy of the developed discrete representation: comparison of the horizontal component of the solid particle velocity v_x calculated by our FD scheme and exact method by Diaz & Ezziani (2008). The FD scheme is capable of sensing an interface no matter what the angle between the interface and grid lines is. The upper panel labelled a is for receiver R_T, the lower panel labelled b is for receiver R_R.

7.3. Two halfspaces with realistic values of the fast P-wave velocities – comparison with an exact solution

As we explained before, the large values of the fast P-wave velocities in the halfspaces and the large value of the velocity contrast at the interface made it possible to perform stringent tests of accuracy and to demonstrate the sub-cell resolution of the developed representation. In order to include also more realistic material parameters we will compare our FD solution with the exact solution for a model of two halfspaces with material parameters specified in Table 2. Note, however, that the material-parameter values in Table 2 do not pose such a stringent accuracy test as the material parameters considered so far.

Except the values of the material parameters we consider the configuration shown in Fig. 2, the A, B and C interface positions shown in Fig. 4, and source-time function shown in Fig. 3. Fig. 10 compares the horizontal component of the particle velocity v_x obtained with our FD modelling and the Gar6more2D code developed by Diaz & Ezziani (2008). The upper panel labelled a is for receiver R_T, the lower panel labelled b is for receiver R_R. In each of the two panels, frame labelled A compares the FD seismogram (in black) and the exact seismogram (red) for the A interface position. Similarly, frames labelled B and C compare the FD and exact seismograms for the B and C interfaces positions. Frame labelled A B C shows the FD seismograms for the 3 positions in order to illustrate the scatter in seismograms due to different positions of the interface within one grid cell. Because the scatter is small – due to realistic low values of the fast P-wave velocities – the lower right frame shows a magnified part of the seismograms. Though small, the differences among seismograms demonstrate the sub-cell resolution of the representation. It is clear from all comparisons that the FD seismograms are in very good agreement with the exact seismograms.

Figure 10. Illustration of accuracy of the developed discrete representation: comparison of the horizontal component of the solid particle velocity v_x calculated by our FD scheme and the exact method by Diaz & Ezziani (2008). The upper panel labelled a is for receiver R_T, the lower panel labelled b is for receiver R_R. Frames labelled A, B and C compare the FD and exact seismograms for the A, B and C positions of the horizontal interface in the grid shown in Fig. 5, respectively. We can see very good agreement between the FD and exact seismograms. Frame labelled A B C shows only FD seismograms for the 3 interface positions in order to illustrate the scatter in seismograms due to different positions of the interface within

a grid cell. Because the scatter is small – due to realistically low values of the fast P-wave velocities – the lower right frame shows a magnified part of the seismograms. Though small, the differences among seismograms demonstrate the sub-cell resolution of the developed representation.

7.4. A model of a lens

It is obvious from the previous tests that our discrete representation is capable to model a planar interface. Here we verify the scheme for a model of a lens, that is, a 2D heterogeneity. Fig. 11 shows geometry of the poroelastic lens inside a homogeneous unbounded poroelastic medium, three receiver profiles and position of the source. Table 2 lists material parameters of the lens (medium 1) and the surrounding medium (medium 2). Fig. 12 shows the used source time function. The effective frequency content of the source signal is up to 20 Hz. The corresponding minimum wavelength is approximately 36m. We compare our FD seismograms with those obtained by discontinuous Galerkin (DG) method, 5th-order accurate both in space and time, using a triangular mesh (de la Puente et al. 2008). The upper, middle and lower panel of Fig. 13 shows the horizontal component of the solid particle velocity at receiver positions along the upper, middle and lower receiver profiles, respectively, shown in Fig. 11. For each receiver position there are 3 seismograms shown: the reference DG seismogram (black) and the FD seismograms for the two different discretizations – one with the grid spacing 3m (green), the other with the grid spacing 1m (red). Time step 0.00016s was used in both cases. Similarly, Fig. 14 compares the vertical component of the solid particle velocity. In both Fig. 13 and Fig. 14 the different solutions are in different colours and the seismograms are superimposed. Thus, we can see very good overall agreement between the DG and FD seismograms. In order to have a more detailed comparison of the three solutions for the most significant parts of seismograms, Figs. 15 and 16 show three-times amplified seismograms in the [0.15, 1.50]s time windows for the horizontal and vertical components of the solid particle velocity, respectively. Fig. 17 shows an analogous picture of the pore pressure. The level of agreement is convincing even in this zoom-out comparison.

		medium 1	medium 2
Solid	Bulk modulus, $K_s\left(GPa\right)$	35.0	35.0
	Density, $\rho_s\left(kg\,m^{-3}\right)$	2650	2650
Matrix	Bulk modulus, $K_m\left(GPa\right)$	5.0	5.0
	Shear modulus, $\mu\left(GPa\right)$	11.0	11.0
	Porosity, ϕ	0.2	0.2
	Tortuosity, T	2.0	2.0
Fluid	Density, $\rho_f\left(kg\,m^{-3}\right)$	70	912
	Viscosity, $\eta\left(Pas\right)$	0.0	0.0
	Bulk modulus, $K_f\left(GPa\right)$	0.077	1.5
Velocity	Fast P-wave $\left(m\,s^{-1}\right)$	3059	3274
	Slow P-wave $\left(m\,s^{-1}\right)$	735	773
	S-wave $\left(m\,s^{-1}\right)$	2274	2230

Table 2. Material parameters describing the second model of two halfspaces with a planar interface and the model of the lens inside an unbounded medium.
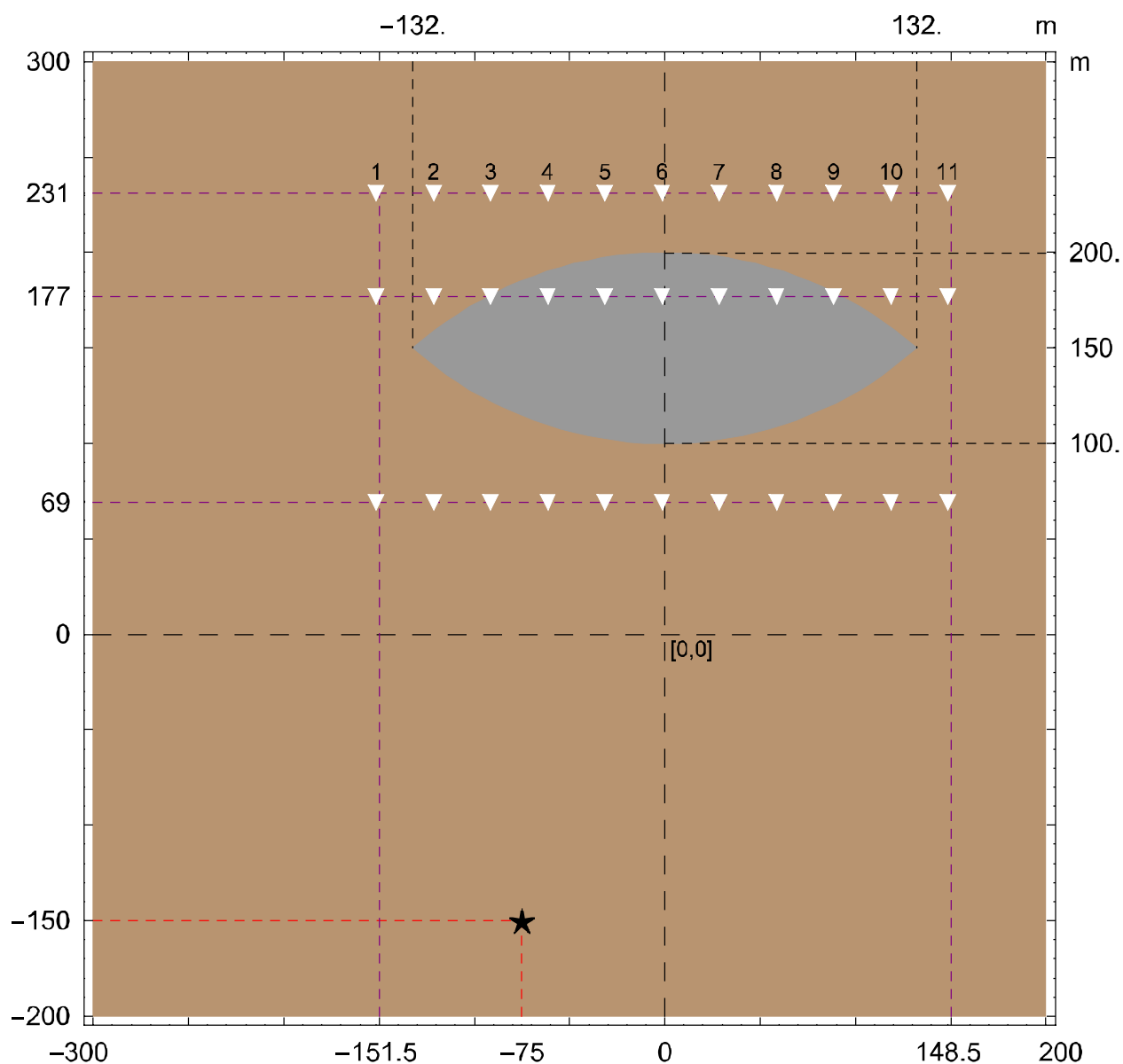
Figure 11. Geometry of the poroelastic lens inside a homogeneous unbounded poroelastic medium, three profiles of receiver positions (white triangles) and position of the source (star).
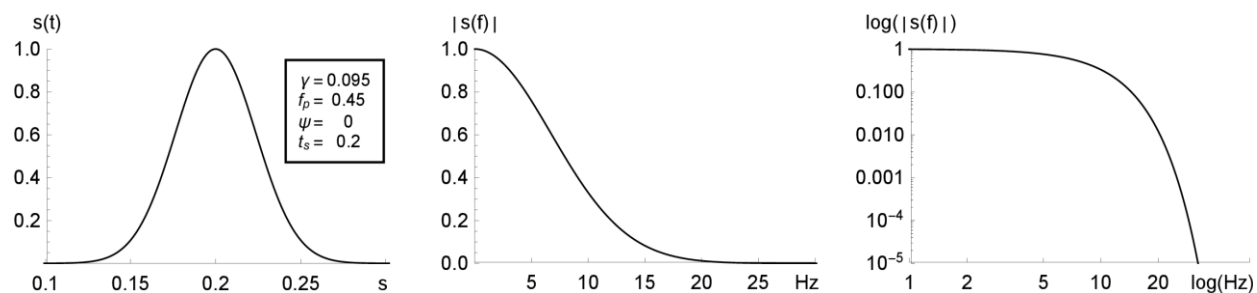
Fig. 12. Source time function used for the problem of the lens, and its amplitude and log Fourier spectra.
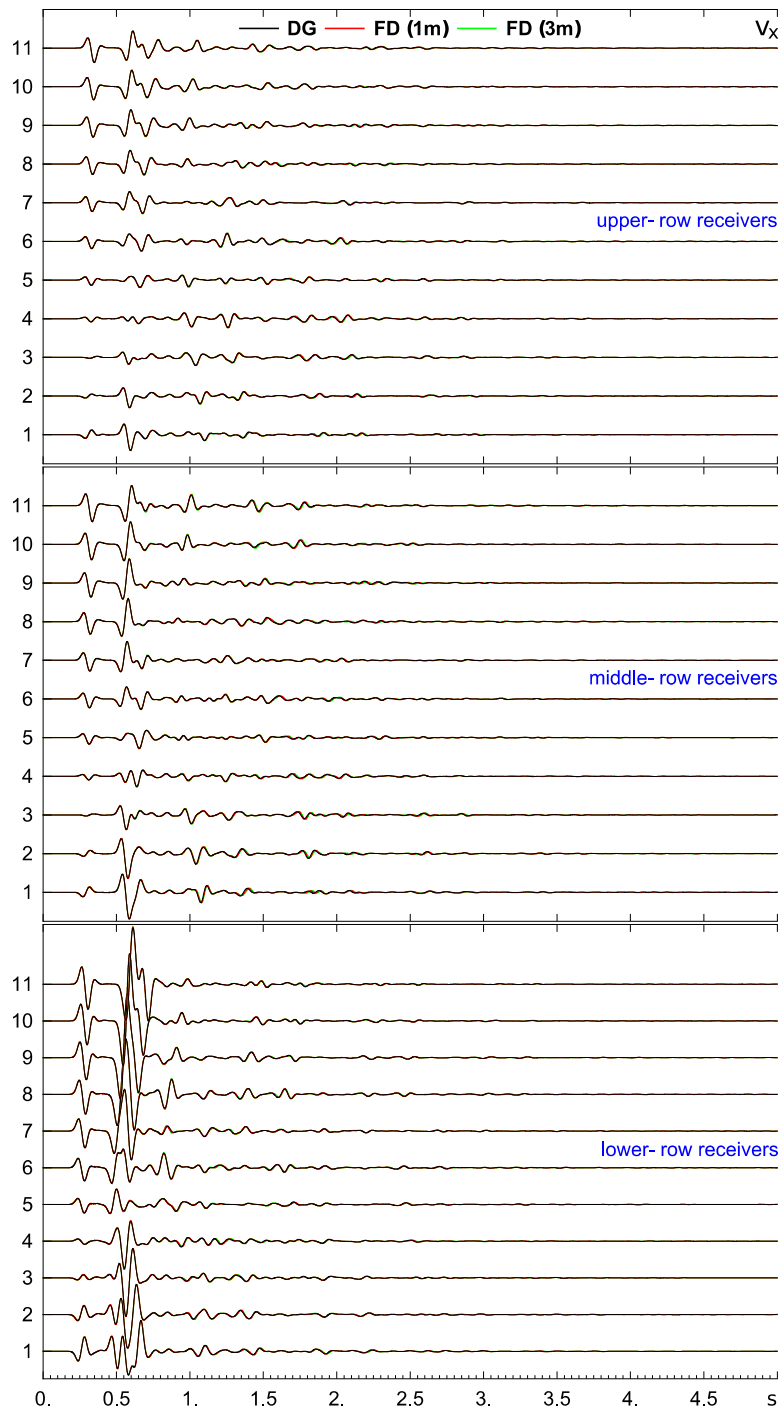
Fig. 13. Horizontal component of the solid particle velocity. Upper, middle and lower panels show seismograms at receivers along the upper, middle and lower receiver profiles (Fig. 11), respectively. For each receiver a seismogram obtained using the discontinuous Galerkin method (DG, in black) is compared with FD seismograms obtained for two values of the grid spacing – 1m (in red) and 3m (in green).
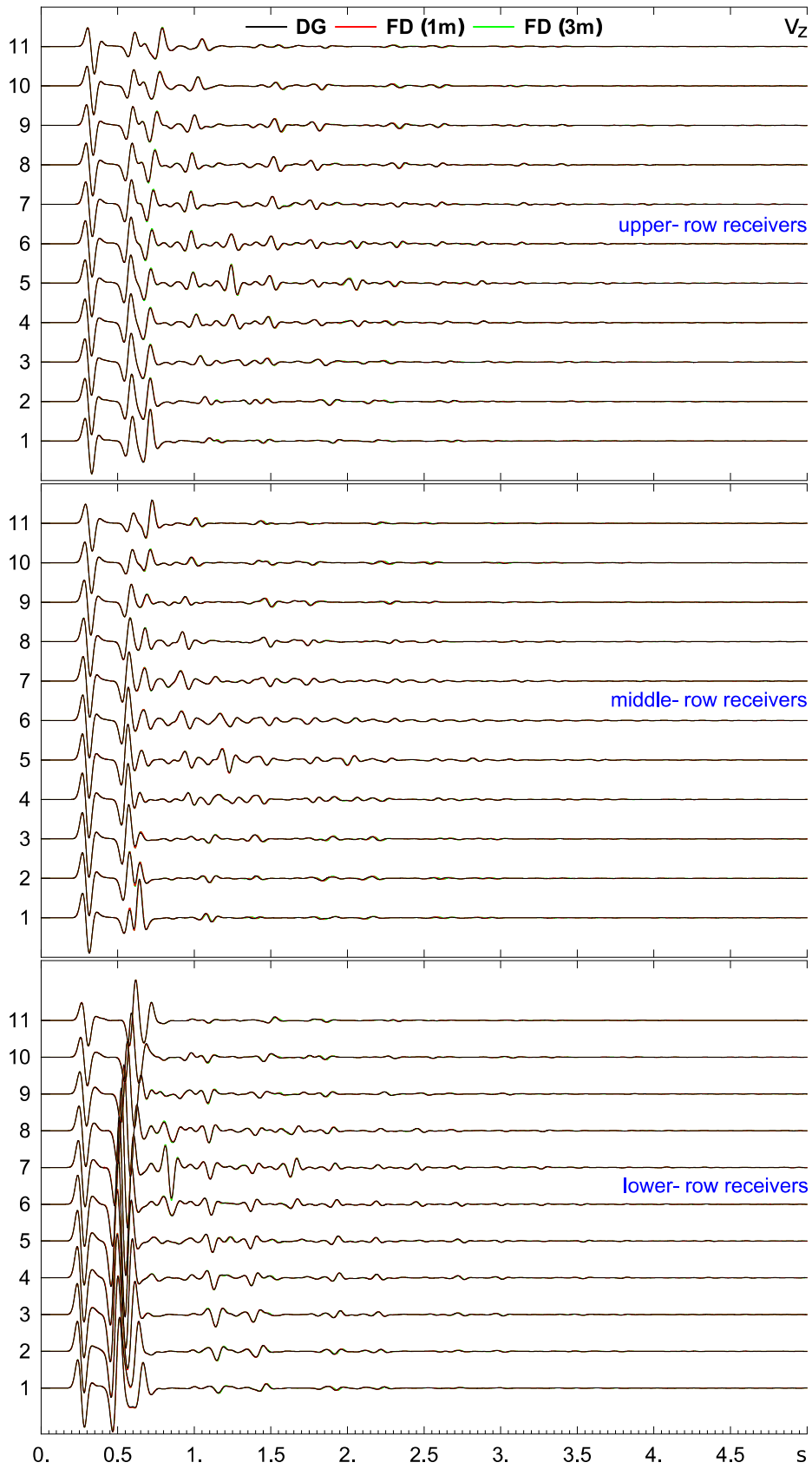
Fig. 14. The same as in Fig. 13 but for the vertical component of the solid particle velocity.
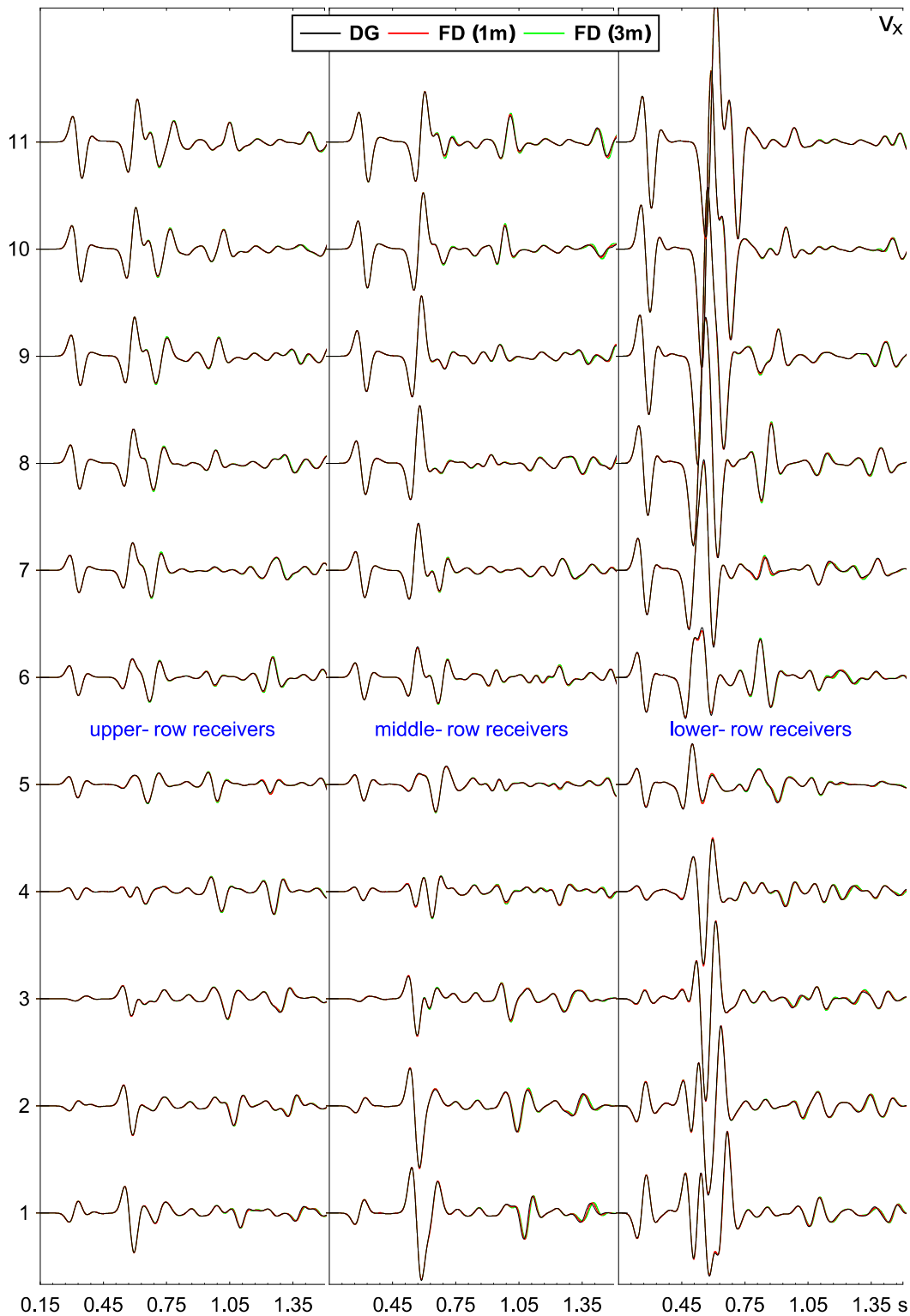
Fig. 15. Horizontal component of the solid particle velocity. Left, central and right panels show seismograms in the [0.15, 1.50]s time windows at receivers along the upper, middle and lower receiver profiles (Fig. 11), respectively. For each receiver a seismogram obtained using the discontinuous Galerkin method (DG, in black) is compared with FD seismograms obtained for two values of the grid spacing – 1m (in red) and 3m (in green). The chosen time windows compare the most significant parts of the seismograms shown in Fig. 13. The amplitudes in this figure are 3 times larger than those in Fig. 13. The FD and DG seismograms are in very good agreement.
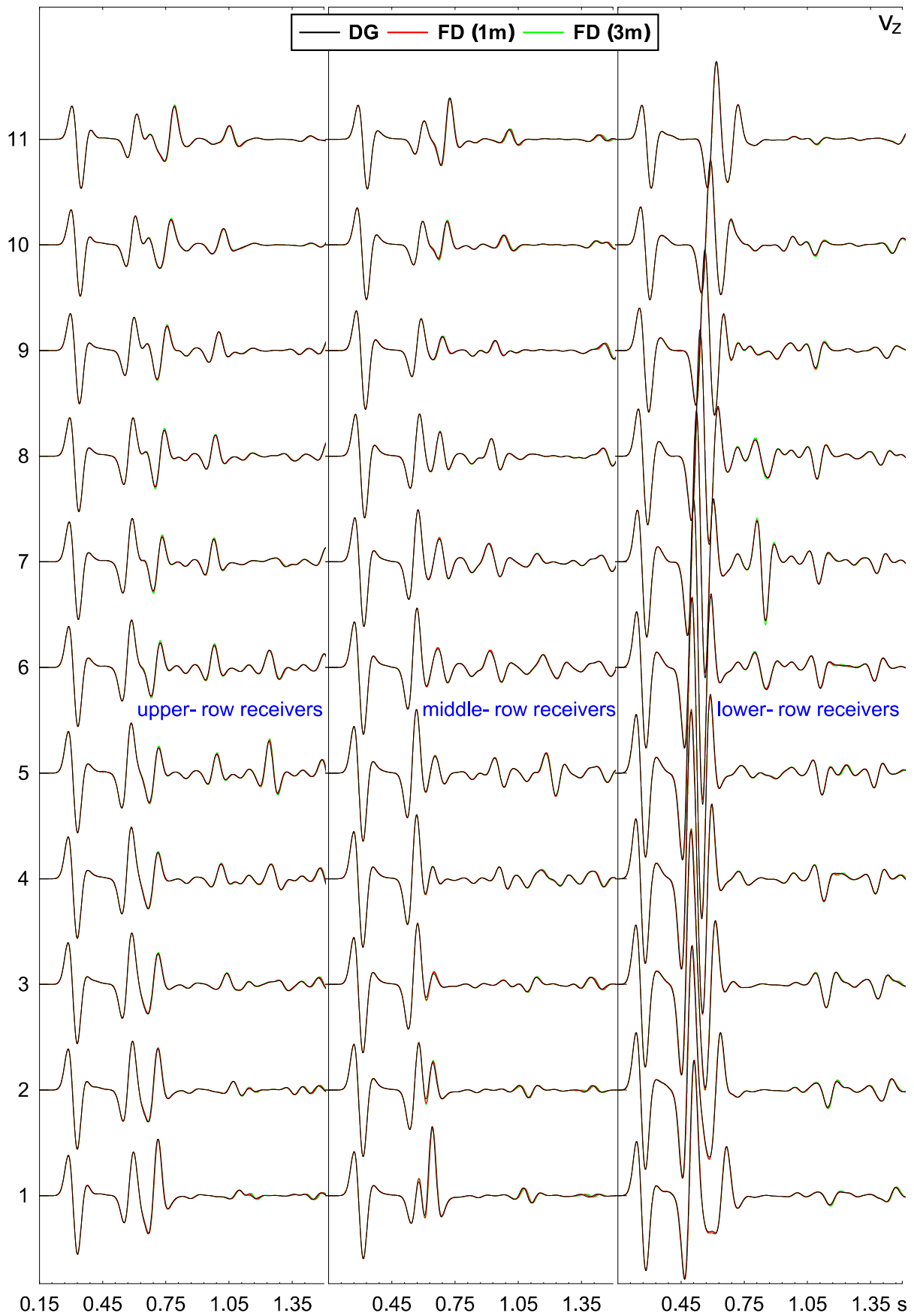
Fig. 16. The same as in Fig. 15 but for the vertical component of the solid particle velocity.
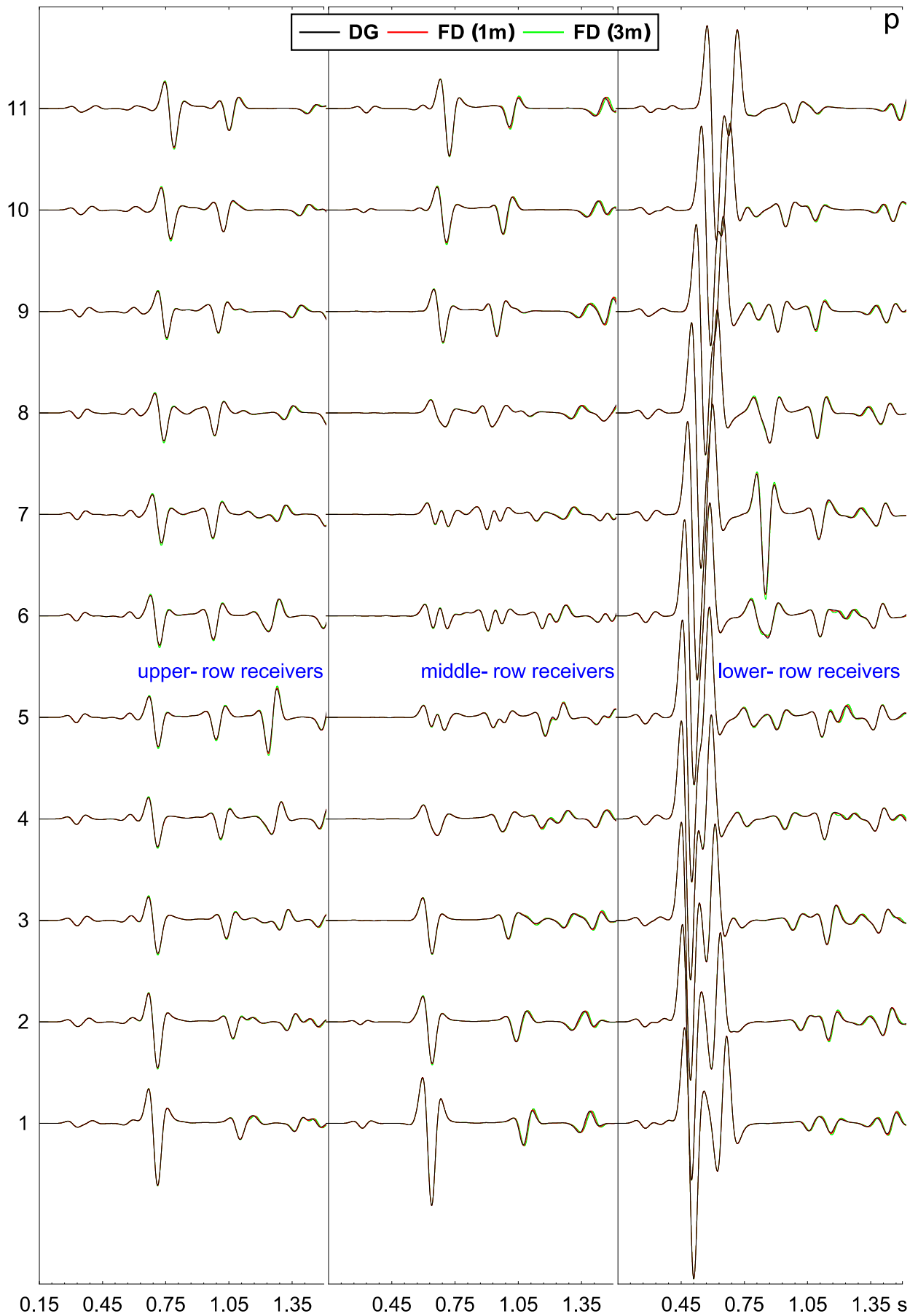
Fig. 17. The same as in Figs 15 and 16 but for the pore pressure.

7.5. Unbounded homogeneous poroelastic medium with non-zero resistive damping

Our goal is to test our discrete representation of material interfaces between poroelastic media with non-zero resistive damping. Because, however, we have not found an independent solution for a model with a material interface between two media with non-zero resistive damping, we split verification into two tests: In the first test we consider an unbounded medium and compare our FD solution with the analytical solution based on the works by Karpfinger et al. (2005, 2009); we have elaborated the corresponding computer code. In the second test we demonstrate the sub-cell resolution of our discrete representation of material interface.

Table 3 shows material parameters of two media. The parameters of the upper halfspace are used for the unbounded medium in the first test.

		upper halfspace	lower halfspace
Solid	Bulk modulus, $K_s \left(GPa \right)$	35.0	35.0
	Density, $\rho_s \left(kg\,m^{-3} \right)$	2650	2650
Matrix	Bulk modulus, $K_m \left(GPa \right)$	5.0	5.0
	Shear modulus, $\mu \left(GPa \right)$	11.0	11.0
	Porosity, ϕ	0.2	0.2
	Tortuosity, T	2.0	2.0
Fluid	Density, $\rho_f \left(kg\,m^{-3} \right)$	912	70
	Viscosity, $\eta \left(\times 10^{-3} Pas \right)$	383	0.025
	Bulk modulus, $K_f \left(GPa \right)$	1.5	0.077
	Permeability, $\kappa \left(\times 10^{-12} m^2 \right)$	1.0	1.0
Velocity at 20 Hz	Fast P-wave $\left(m\,s^{-1} \right)$	3262	3057
	Slow P-wave $\left(m\,s^{-1} \right)$	2	75
	S-wave $\left(m\,s^{-1} \right)$	2186	2270

Table 3. Material parameters describing models in the first and second tests for poroelastic media with non-zero resistive damping. The parameters of the upper halfspace are used also for the unbounded medium in the first test. The velocity as a function of frequency is given by Carcione (2015).

The source-receiver configuration for a 2D modelling is shown in Fig. 18. The source-time function is shown in Fig. 19.
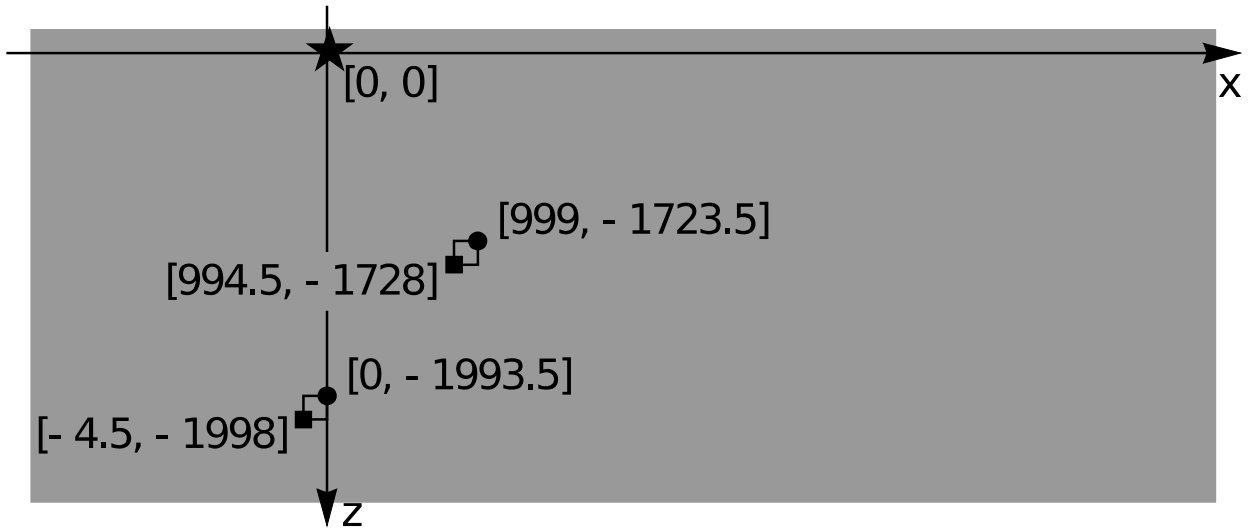

Figure 18. Schematic presentation of the source-receiver configuration in the unbounded poroelastic medium with non-zero resistive damping. Position of the point of intersection of the computational plane with a perpendicular line source generating only compressional waves is indicated by a star. Positions of the receivers for the v_x and v_z solid particle-velocity components are indicated by solid squares and circles, respectively (their positions differ due to the staggered grid). The depicted coordinate system serves only for simple indication of relative positions of the source, receivers and interface.
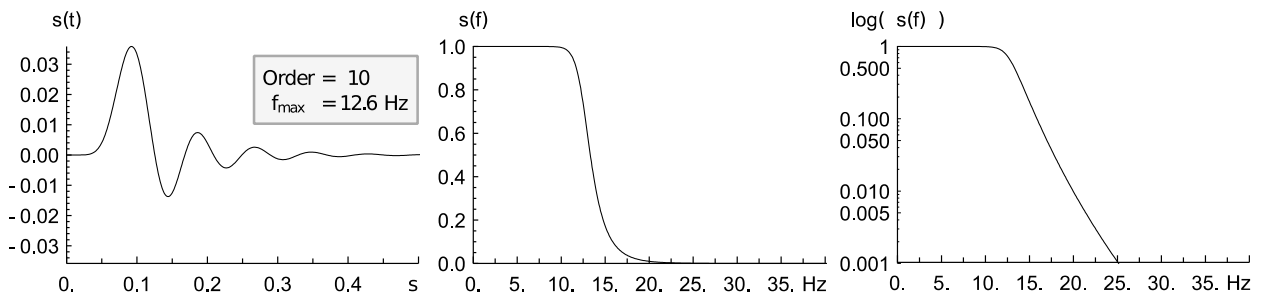
Figure 19. Source time function, and its amplitude and log Fourier spectra.
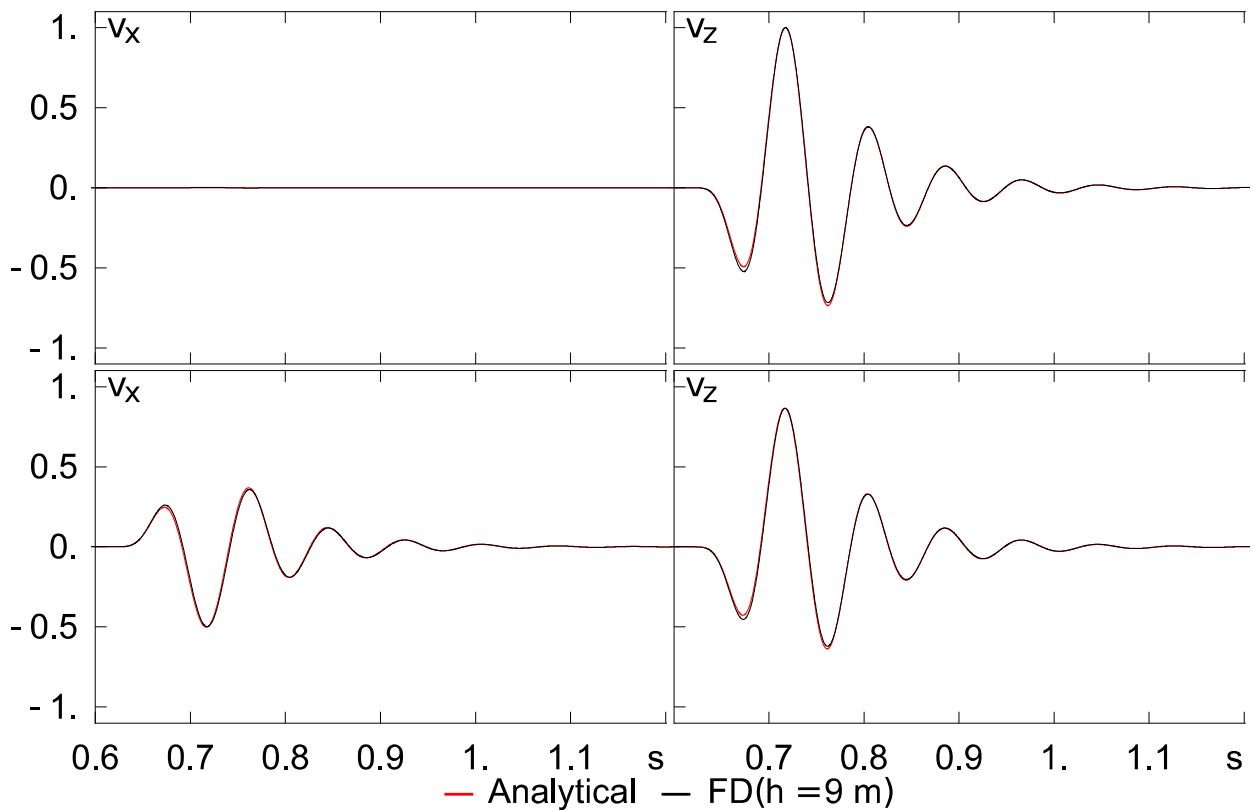
Figure 20. The first test: comparison of our FD solution with the analytical solution based on the works by Karpfinger et al. (2005, 2009) for the unbounded homogeneous poroelastic medium with non-zero resistive damping.

Fig. 20 shows comparison of our FD seismograms with those obtained using the exact method developed by Karpfinger et al. (2005, 2009). Note that the analytical solution is calculated in the frequency domain and then converted to the time domain using the inverse Fourier transform. The level of agreement between the two solutions is very good.

7.6. Two halfspaces with a planar interface parallel with a grid plane – the case of non-zero resistive damping

As explained in the beginning of the previous section, for the model of an interface between two poroelastic media with non-zero resistive damping we have only our FD solution available. The presented test is, however, important because it convincingly demonstrates the sub-cell resolution of the developed discrete representation of the interface also in media with non-zero resistive damping.

We consider a planar contact of two media. Material parameters in the upper and lower halfspaces are shown in Table 3, schematic configuration of the source, receiver positions and interface in Fig. 21, and four positions of the interface within one half of the grid spacing in Fig. 22. The source-time function is the same as in the previous test, see Fig. 19.

Fig. 23 compares FD seismograms, v_x component of the solid article velocity, for four positions of the material interface. As explained in the legend of Fig. 23, the comparison clearly demonstrates the sub-cell resolution of the developed discrete representation of the material interface also for media with non-zero resistive damping.
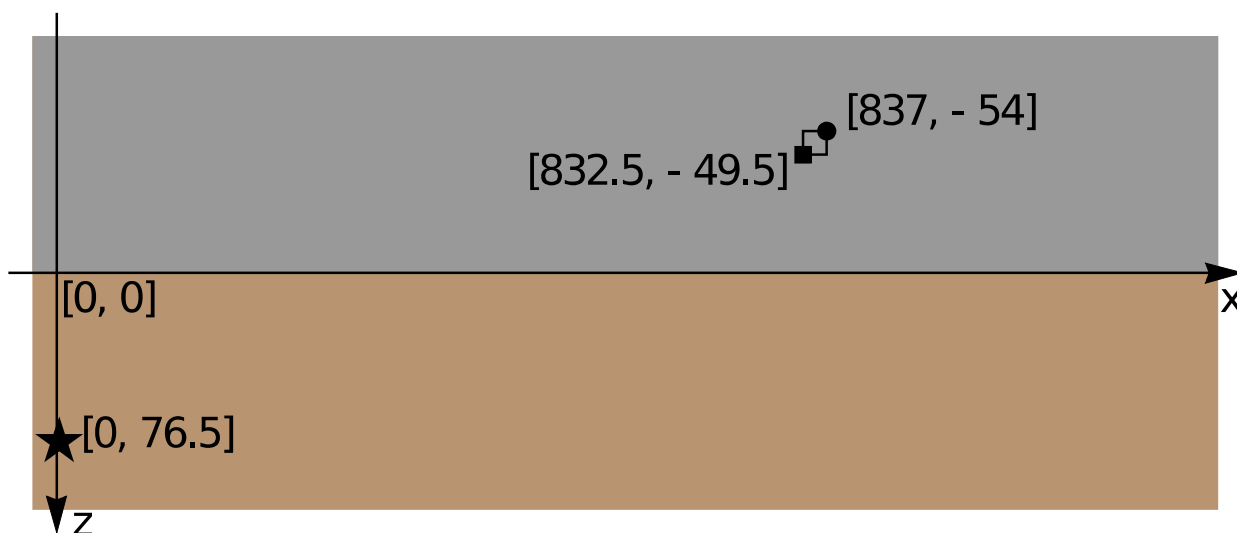

Figure 21. Schematic presentation of the model with the horizontal interface between two poroelastic halfspaces with non-zero resistive damping. Position of the point of intersection of the computational plane with a perpendicular line source generating only compressional waves is indicated by a star. Positions of the receivers for the v_x and v_z solid particle-velocity components are indicated by solid squares and circles, respectively (their positions differ due to the staggered grid). The depicted coordinate system serves only for simple indication of relative positions of the source, receivers and interface.
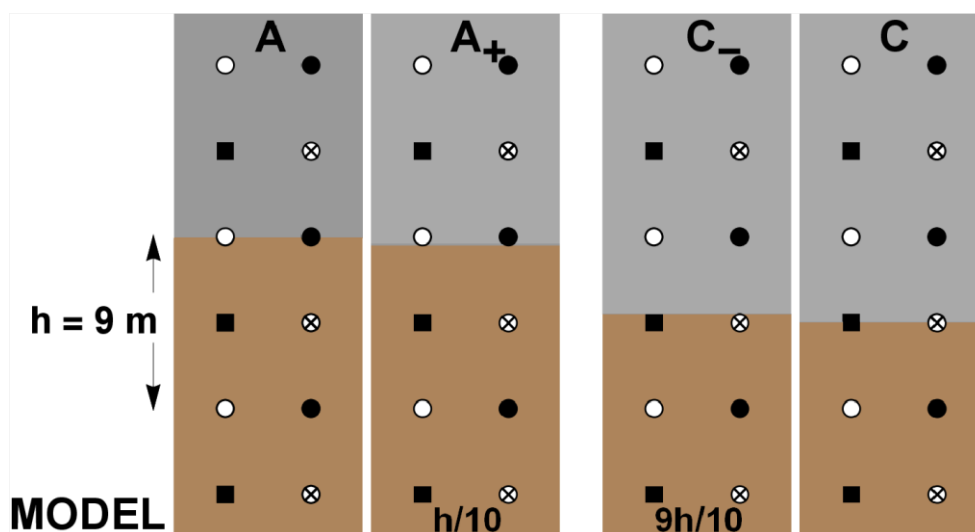

Figure 22. 4 different positions of the interface (schematically shown in Fig. 21) within one half of the grid spacing h. Two positions of the interface with respect to the spatial grid, A and C, correspond to positions considered in Fig. 4. Seismograms in for these two positions are compared in Fig. 23 with seismograms for positions A_+ and C_- that are just $h/10$ away from positions A and C, respectively. The source and receivers are at the same positions in the grid in all 4 cases.
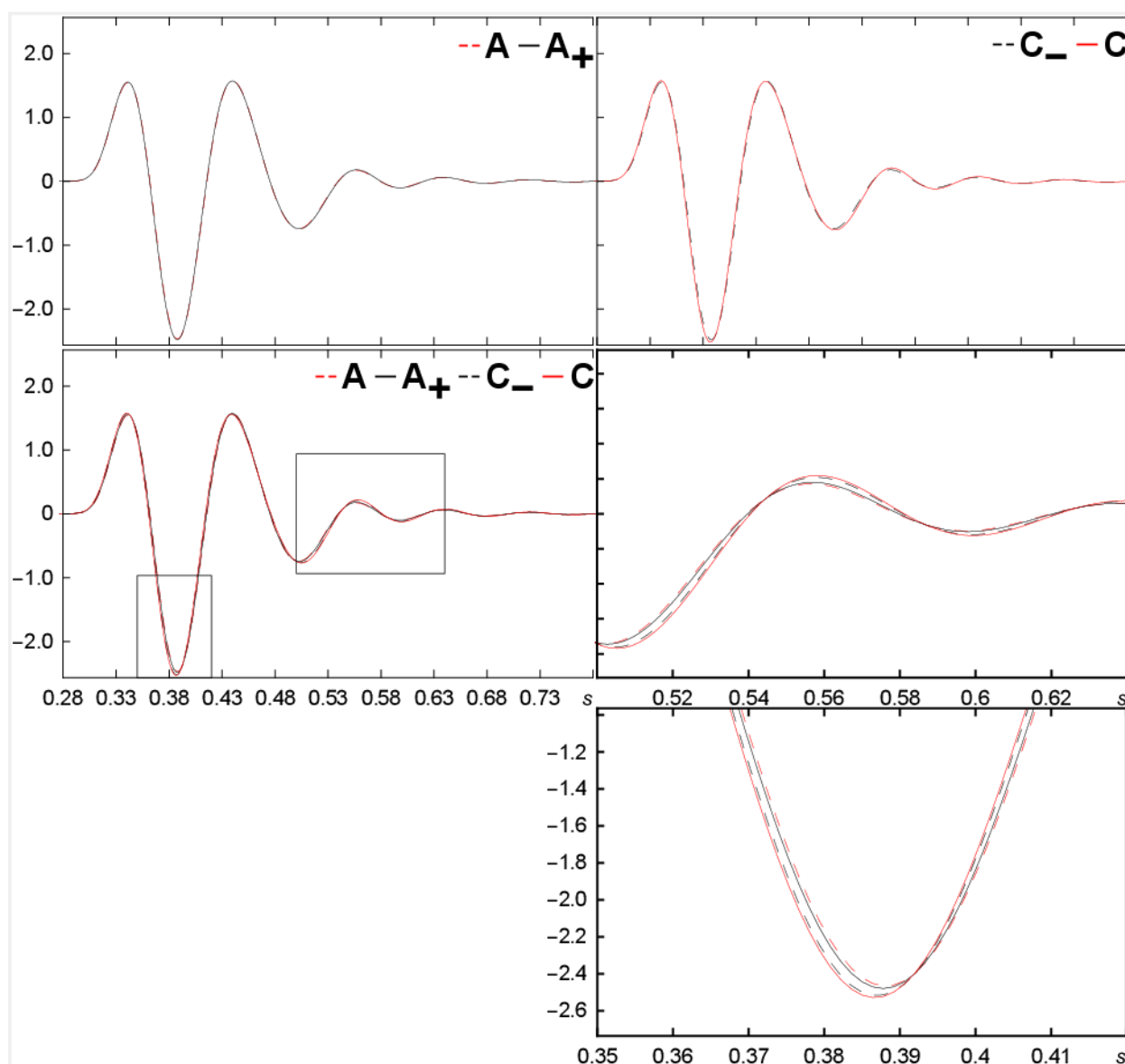
Figure 23. Comparison of our FD solutions (v_x) for the 4 interface positions, A, A$_+$, C$_-$ and C, shown in Fig. 22. Because the distance between interface positions A and A$_+$, and positions C and C$_-$, is just one-tenth of the grid spacing, $h/10$, seismogram for A should be close to seismogram for A$_+$, and, analogously, seismogram for C should be close to seismogram for C$_-$. This is shown in the upper row of the figure. Because distance between interface positions A and C is $h/2$, we should clearly see a difference between seismograms for A and C. Moreover, we should also see that this difference is larger than the differences between seismograms for A and A$_+$ or seismograms for C and C$_+$. This is obvious from comparison in frame labelled A A$_+$ C$_-$ C and two magnified parts of seismograms. This illustrates the sub-cell resolution of the developed representation also for media with non-zero resistive damping.

8 CONCLUSIONS

We have developed a discrete representation of a strong material heterogeneity in the poroelastic medium. The representation makes it possible to model an arbitrary shape and position of an interface with sub-cell resolution in the spatial grid. The computational efficiency of the finite-difference grid is unchanged compared to the scheme for a homogeneous and smoothly heterogeneous medium because the number of operations for updating stress-tensor, fluid pressure and particle velocities is the same. The only difference is that it is necessary to evaluate averaged grid material parameters once before the finite-difference simulation itself. Thus, the developed representation extends the possibilities of the finite-difference modelling of seismic wave propagation in the poroelastic medium similarly as the representations developed for the elastic and viscoelastic media (Moczo et al. 2002, 2014; Kristek and Moczo 2003; Kristek et al 2017).

REFERENCES

Alterman, Z. S. & Karal, F.C., 1968. Propagation of elastic waves in layered media by finite difference methods, *Bull. Seism. Soc. Am.*, **58**, 367-398.

Andrews, D. J., 1973. A numerical study of tectonic stress release by underground explosions, *Bull. Seism. Soc. Am.*, **63**, 1375-1391.

Blanc, E., 2013. Time-domain numerical modeling of poroelastic waves: the Biot-JKD model with fractional derivatives, *Thèse*, Aix-Marseille Université, 157 pp.

Carcione, J.M., 1998. Viscoelastic effective rheologies for modelling wave propagation in porous media, *Geophys. Prosp.*, **46**, 249-270.

Carcione, J.M., 2015. Wave Fields in Real Media: Wave Propagation in Anisotropic, Anelastic, Porous and Electromagnetic Media, Third edition, *Elsevier*.

Carcione, J.M. & Helle, H.B., 1999. Numerical Solution of the Poroviscoelastic Wave Equation on a Staggered Mesh, *J. Comp. Phys.*, **154**, 520-527.

Carcione, J.M., Morency, C. & Santos, J.E., 2010. Computational poroelasticity – A review, *Geophysics*, **75**, 75A229-75A243.

Carcione, J.M. & Quiroga-Goode, G., 1995. Some aspects of the physics and numerical modelling of Biot compressional waves, *J. Comp. Acoustics*, **3**(4), 261-280.

Chaljub, E., Maufroy, E., Moczo, P., Kristek, J., Hollender, F., Bard, P.-Y., Priolo, E., Klin, P., de Martin, F., Zhang, Z., Zhang, W. & Chen, X., 2015. 3D numerical simulations of earthquake ground motion in sedimentary basins: testing accuracy through stringent models, *Geophys. J. Int.*, **201**, 90–111.

Chaljub, E., Moczo, P., Tsuno, S., Bard, P.-Y., Kristek, J., Käser, M., Stupazzini, M. & Kristekova, M., 2010. Quantitative comparison of four numerical predictions of 3D ground motion in the Grenoble Valley, France, *Bull. Seism. Soc. Am.*, **100**, 1427-1455.

Chiavassa, G., & Lombard, B., 2011. Time domain numerical modeling of wave propagation in 2D heterogeneous porous media, *J. Comput. Phys.* **230**, 5288–5309.

Chiavassa, G. & Lombard, B., 2013. Wave Propagation Across Acoustic/Biot's Media: A Finite-Difference Method, *Commun. Comput. Phys.*, **14** (4), 985-1012.

De la Puente, J., Dumbser, M., Käser, M. & Igel, H., 2008. Discontinuous Galerkin methods for wave propagation in poroelastic media, *Geophysics*, **73**(5), pp. T77-97.

Deresiewicz, H. & Skalak, R., 1963. On uniqueness in dynamic poroelasticity, *Bull. Seism. Soc. Am.*, **53**, 783–788.

Dai, N., Vafidis, A. & Kanasewich, E., 1995. Wave propagation in heterogeneous porous media: a velocity-stress, finite-difference method, *Geophysics*, **60**(2), 327–340.

Diaz, J. & Ezziani, A., 2008. Analytical Solution for Wave Propagation in Stratified Poroelastic Medium. Part I: the 2D Case, *Rapport de recherché* No 6591, INRIA.

Garg, S. K., Nayfeh, A. H., & Good, A. J., 1974. Compressional waves in fluid-saturated elastic porous media, *J. Appl. Phys.* **45**, 1968–1974.

Graves, R. W., 1996. Simulating seismic wave propagation in 3D elastic media using staggered-grid finite differences, *Bull. Seism. Soc. Am.*, **86**(4), 1091-1106.

Gurevich, B. & Schoenberg, M., 1999. Interface conditions for Biot's equations of poroelasticity, *J. Acoust. Soc. Am.*, **105**, 2585-2589.

Hassanzadeh, S., 1991. Acoustic modeling in fluid saturated porous media, *Geophysics*, **56**(4), 424–435.

Karpfinger, F., Müller, T.M. & Gurevich, B., 2005. Radiation patterns of seismic waves in poroelastic media, *SEG/Houston 2005 Annual Meeting, Technical Program Expanded Abstracts*, SMP1.4, 1791-1795.

Karpfinger, F., Müller, T.M. & Gurevich, B., 2005. Green's functions and radiation patterns in poroelastic solids revisited, *Geophys. J. Int.*, **178**, 327-337.

Kelly, K. R., Ward, R.W., Treitel, S.R. & Alford, M., 1976. Synthetic seismograms: A finite-difference approach, *Geophysics*, **41**, 2-27.

Kristek, J. & Moczo, P., 2003. Seismic-wave propagation in viscoelastic media with material discontinuities: A 3D fourth-order staggered-grid finite-difference modelling, *Bull. Seism. Soc. Am.*, **93**, 2273-2280.

Kristek, J. & Moczo, P., 2014. FDSim3D – The Fortran95 Code for Numerical Simulation of Seismic Wave Propagation in 3D Heterogeneous Viscoelastic Media. www.cambridge.org/moczo

Kristek, J., Moczo, P., Chaljub, E. & Kristekova, M., 2017. An orthorhombic representation of a heterogeneous medium for the finite-difference modelling of seismic wave propagation, *Geophys. J. Int.*, **208**, 1250-1264.

Kristekova, M., Kristek, J. & Moczo, P., 2009. Time-frequency misfit and goodness-of-fit criteria for quantitative comparison of time signals, *Geophys. J. Int.*, **178**, 813-825.

Krzikalla, F. & Müller, T.M., 2007a. Simulation of Wave Propagation in Poroelastic Structures Using a Modified Finite-Difference Scheme. EAGE 69th Conference & Exhibition, P327.

Krzikalla, F. & Müller, T.M., 2007b. High-contrast finite-differences modeling in heterogeneous poroelastic media, 77th Annual International Meeting, SEG, *Expanded Abstracts*, 2030–2034.

Lovera, O.M., 1987. Boundary conditions for a fluid-saturated porous solid, *Geophysics*, **52**, 174-178.

Masson,Y.J. & Pride, S.R., 2007. Poroelastic finite difference modeling of seismic attenuation and dispersion due to mesoscopic-scale heterogeneity, *J. geophys. Res.*, **112**, B03204.

Masson, Y.J. & Pride, S.R., 2010. Finite-difference modeling of Biot's poroelastic equations across all frequencies, *Geophysics*, **75**(2), N33–N41.

Masson, Y.J., Pride, S.R. & Nihei, K.T., 2006. Finite-difference modeling of Biot's poroelastic equations at seismic frequencies, *J. geophys. Res.*, **111**, B10305,

Maufroy, E., Chaljub, E., Hollender, F., Kristek, J., Moczo, P., Klin, P., Priolo, E., Iwaki, A., Iwata, T., Etienne, V., De Martin, F., Theodoulidis N.P., Manakou, M., Guyonnet-Benaize, C., Pitilakis, K. & Bard, P.-Y., V. 2015. Earthquake ground motion in the Mygdonian basin, Greece: the E2VP verification and validation of 3D numerical simulation up to 4 Hz, *Bull. Seism. Soc. Am.*, **105**, 1398-1418.

Min, D.J., Shin, C., Kwon, B.D. & Chung, S., 2000. Improved frequency-domain elastic wave modeling using weighted-averaging difference operators, *Geophysics*, **65**(3), 884–895.

Moczo, P., Kristek, J. & Galis, M., 2014. The finite-difference modelling of earthquake motions: Waves and ruptures, *Cambridge University Press*.

Moczo, P., Kristek, J., Vavryčuk, V., Archuleta, R.J. & Halada, L., 2002. 3D heterogeneous staggered-grid finite-difference modeling of seismic motion with volume harmonic and arithmetic averaging of elastic moduli and densities, *Bull. Seism. Soc. Am.*, **92**, 3042-3066.

Morency, Ch. & Tromp, J., 2008. Spectral-element simulations of wave propagation in porous media, *Geophys. J. Int.*, **175**, 301-345.

O'Brien, G., 2010. 3D rotated and standard staggered finite-difference solutions to Biot's poroelastic wave equations: Stability condition and dispersion analysis, *Geophysics*, **75**, T111-T119.

Riney, T.D, Dienes, J.K., Plazier, C.A., Garg, S.K., Kirsch, J.W., Brownell, D.H. & Good, A.J., 1972. Ground Motion Models and Computer Techniques, Formal Report under Contract No. DASA 01-69-C-0159(P0Ü003), *S Report 3SR-1071* (unpublished)

Riney, T.D., Frazier, G.A., Garg, S.K., Good, A.J., Herrmann, R.G., Morland, L.W., Pritchett, J. W., Rice, M.H. & Sweet, J., 1973. Constitutive models and computer techniques for gorund motion predictions. *Systems, Science and Software Report* No. SSS-R-73-1490, 357 pp. (unpublished).

Saenger, E.H., Krüger, O.S. & Shapiro, S.A., 2004. Numerical considerations of fluid effects on wave propagation: Influence of the tortuosity, *Geophys. Res. Lett.*, **31**, L21613.

Saenger, E.H., Shapiro, S.A. & Keehm, Y., 2005. Seismic effects of viscous Biot-coupling: Finite difference simulations on micro-scale, *Geophys. Res. Lett.*, **32**, L14310.

Sheen, D.-H., Tuncay, K., Baag, C.-E. & Ortoleva, P.J., 2006. Parallel implementation of a velocity-stress staggered-grid finite-differences method for 2D poroelastic wave propagation: *Computers & Geosciences*, **32**, 1182–1191.

Wang, X., Zhang, H. & Wang, D., 2003. Modelling seismic wave propagation in heterogeneous poroelastic media using a high-order staggered finite-difference method, *Chinese J. Geophysics*, **46**, 1206-1217.

Yang, Q. & Mao, W., 2017. Simulation of seismic wave propagation in 2-D poroelastic media using weighted-averaging finite difference stencils in the frequency–space domain, *Geophys. J. Int.*, **208**, 148-161.

Zeng, Y. Q., He, J.Q. & Liu, Q.H., 2001. The application of the perfectly matched layer in numerical modeling of wave propagation in poroelastic media, *Geophysics*, **66**, 1258-1266.

Zeng, Q. Z. & Liu, Q.H., 2001. A staggered-grid finite-difference method with perfectly matched layers for poroelastic wave equations, *J. Acoust. Soc. Am.*, **109**, 2571-2580.

Zhang, J., 1999. Quadrangle-grid velocity-stress finite difference method for poroelastic wave equations, *Geophys. J. Int.*, **139**, 171–182.

Zhu, X. & McMechan, G.A., 1991. Numerical simulation of seismic responses of poroelastic reservoirs using Biot theory, *Geophysics* **56**, 328-339.

Appendix A

Partitioned FD scheme

Instead of schemes (5.18) and (5.19) the following partitioned schemes are applied in numerical simulations for poroelastic media with non-zero resistive damping, that is non-zero b in Eqs. (5.1):

$$
\begin{aligned}
VX_{I,L+1/2}^{n+1/2} &= VX_{I,L+1/2}^{*} + \frac{1}{\left\langle S^x \right\rangle_{I,L+1/2}^{z}} \frac{\Delta}{h} \\
&\left\{ \left\langle F^x \right\rangle_{I,L+1/2}^{z} \left[D_x^{(4)} TXX_{I,L+1/2}^{n} + D_z^{(4)} TXZ_{I,L+1/2}^{n} \right] \right. \\
&\left. + \left\langle G^x \right\rangle_{I,L+1/2}^{z} D_x^{(4)} P_{I,L+1/2}^{n} \right\}
\end{aligned}
\tag{A.1}
$$

$$VX^*_{I,L+1/2} = VX^{n-1/2}_{I,L+1/2} +$$

$$\frac{1}{\langle P^x \rangle^z_{I,L+1/2}} \left\{ 1 - \exp\left[-\Delta \left(\frac{\langle P^x \rangle^z \langle H^x \rangle^z}{\langle S^x \rangle^z} \right)_{I,L+1/2} \right] \right\} QX^{n-1/2}_{I,L+1/2} \qquad (A.2)$$

$$QX^{n+1/2}_{I,L+1/2} = QX^*_{I,L+1/2} -$$

$$- \frac{1}{\langle S^x \rangle^z_{I,L+1/2}} \frac{\Delta}{h}$$

$$\left\{ \left(\langle R^x \rangle^z \left\langle \frac{G^x}{R^x} \right\rangle^z \right)_{I,L+1/2} \left[D^{(4)}_x TXX^n_{I,L+1/2} + D^{(4)}_z TXZ^n_{I,L+1/2} \right] \qquad (A.3) \right.$$

$$\left. + \left(\langle P^x \rangle^z \langle G^x \rangle^z \right)_{I,L+1/2} D^{(4)}_x P^n_{I,L+1/2} \right\}$$

$$QX^*_{I,L+1/2} = \exp\left[-\Delta \left(\frac{\langle P^x \rangle^z \langle H^x \rangle^z}{\langle S^x \rangle^z} \right)_{I,L+1/2} \right] QX^{n-1/2}_{I,L+1/2} \qquad (A.4)$$

The FD schemes (5.20) and (5.21), that is the discrete approximations of the constitutive relations, remain unchanged.